MNRAS 000, 1–?? (2015) Preprint 28 June 2021 Compiled using MNRAS LATEX style file v3.0

The ionised gas outflow in the Circinus galaxy: kinematics and physical conditions

M. A. Fonseca-Faria[1],★ A. Rodríguez-Ardila[1,2], M. Contini[3], V. Reynaldi[4]
[1] INPE - Instituto Nacional de Pesquisas Espaciais, Av. dos Astronautas, CEP 12227-010, São José dos Campos - SP, Brazil
[2] Laboratório Nacional de Astrofísica - Rua dos Estados Unidos 154, Bairro das Nações . CEP 37504-364, Itajubá, MG, Brazil
[3] School of Physics and Astronomy, Tel Aviv University, Tel Aviv 69978, Israel.
[4] Facultad de Ciencias Astronómicas y Geofísicas - Universidad Nacional de La Plata, La Plata, Argentina

Accepted XXX. Received YYY; in original form ZZZ

ABSTRACT

We employ MUSE/VLT data to study the ionised and highly ionised gas phases of the feedback in Circinus, the closest Seyfert 2 galaxy to us. The analysis of the nebular emission allowed us to detect a remarkable high-ionisation gas outflow beyond the galaxy plane traced by the coronal lines [Fe VII] λ6089 and [Fe X] λ6374, extending up to 700 pc and 350 pc NW from the nucleus, respectively. This is the first time that the [Fe X] emission is observed at such distances from the central engine in an AGN. The gas kinematics reveals expanding gas shells with velocities of a few hundred km s^{-1}, spatially coincident with prominent hard X-ray emission detected by Chandra. Density and temperature sensitive line ratios show that the extended high-ionisation gas is characterized by a temperature reaching 25000 K and an electron density $> 10^2$ cm^{-3} . We found that local gas excitation by shocks produced by the passage of a radio jet leads to the spectacular high-ionisation emission in this object. This hypothesis is fully supported by photoionisation models that accounts for the combined effects of the central engine and shocks. They reproduce the observed emission line spectrum at different locations inside and outside of the NW ionisation cone. The energetic outflow produced by the radio jet is spatially located close to an extended molecular outflow recently reported using ALMA which suggests that they both represent different phases of the same feedback process acting on the AGN.

Key words: galaxies: individual: Circinus – line: formation – galaxies: jets – galaxies: Seyfert

1 INTRODUCTION

Outflows from active galactic nuclei (AGN) expel part of the gas surrounding the accretion disc transporting energy and matter to different regions of the host galaxy. Starting from the broad line region (BLR), they cross the narrow line region (NLR) and the galaxy disc, reaching the outermost regions at tens of kpc from the galaxy centre. The energy carried out by the outflowing gas is transmitted to different environments and distances throughout the galaxy, leaving its signature into the different medium phases: ionised, molecular and neutral (Wada et al. 2018). Classic examples of AGN where outflows have been detected in the three phases are the Seyfert 2 galaxies IC 5063 (Dasyra et al. 2015, 2016; Oosterloo et al. 2017) and NGC 5643 (García-Bernete et al. 2020). Outflows from AGN are directly related to the feedback modes currently identified in these sources. They can be of radiative or kinematic origin. Radiative feedback (or quasar feedback mode) results from winds generated by radiation pressure very close to the optically thick accretion disc. They are usually associated to luminous AGN approaching the Eddington limit (Valentini et al. 2020), $L_{Edd} \cong 1.3 \times 10^{38}(M_{BH})/M\odot$ erg s^{-1} (Frank et al. 2002)). These winds can leave the BRL region and propagate over to large distances at galactic scales. Kinematic feedback (or jet feedback) is associated to the kinetic energy transported by the radio jet as in radio galaxies. In this case, the jets may extend over dozens of kpc away from the galaxy core. The mechanical contribution of the jet to the host galaxy is of little relevance (Morganti et al. 2015) as it affects mostly the intergalactic medium. In contrast, radio-quiet objects show weaker jets, of sizes less than a few kpc. They mechanically contribute to the outflows within the host galaxy.

Recently, with the use of integral field unit (IFU) data from MUSE/VLT (Multi Unit Spectroscopic Explorer), it was identified for the first time the highly ionised component of the outflowing gas in the Circinus galaxy. Earlier, this component was only studied by means of the [O III] line data (Mingozzi et al. 2019). Rodríguez-Ardila & Fonseca-Faria (2020) reported the discovery of an extended high ionisation gas outflow in Circinus by means of the [Fe VII] λ6087 line, detected up to a distance of 700 pc from the central source. To explain the structure of the outflow, the au-

★ E-mail: marcosfonsecafaria@gmail.com

thors propose the existence of an expanding shell of gas formed by the interaction of the radio jet with the interstellar gas.

The choice of the Circinus galaxy for the present investigation is not by chance. Circinus is the closest Seyfert 2, located at a distance of 4.2 ± 0.8 Mpc (Freeman et al. 1977), with a projected scale of 1" = 20 pc. It is hosted by a spiral galaxy of SAb morphology and an inclination angle of approximately 65°. The supermassive black hole lurking at the centre of the galaxy has a mass of $1.7 \pm 0.3 \times 10^6$ M$_\odot$ (Greenhill et al. 2003). An outstanding cone-shaped outflow extending to kpc distances is easily visible in the [O III] λ5007 line (Müller Sánchez et al. 2006). The global star formation rate has been measured between 3 and 8 M$_\odot$ yr^{-1} (For et al. 2012) and in the most central regions (< 100 pc) the star formation rate is even smaller (0.1 M$_\odot$ yr^{-1}, Esquej et al. 2014). The observations show a molecular gas outflow from Circinus with velocities consistent with those of the ionised gas outflow (Zschaechner et al. 2016). However, no conclusive evidence exists so far that both are produced by the same mechanism. There is also evidence of a radio jet with a PA (position angle) of 295° ± 5° (Elmouttie et al. 1998). The nuclear spectrum displays prominent high ionisation lines including [Fe VII], [Fe X] and [Fe XIV] in the optical (Oliva et al. 1999), [S IX], [Si VI] and [Ca VIII] in the NIR and [Ne V] in the MIR (Storchi-Bergmann et al. 1999).

In this work we carry out a detailed analysis of the physical conditions of the highly-ionised gas (HIG) component in Circinus, its kinematics and ionisation structure. Our aim is to explore scenarios that best explain the spectacular extension of that component, which reaches a projected linear extension of 700 pc from the AGN. In Sect. 2 we describe the observations, the data treatment and the emission gas distribution and morphology. Sect. 3 deals with the physical conditions of the gas and in Sect. 4 we study the stellar and gas kinematics. The outflow properties are derived in Sect 5. The photoionisation models used to reproduce the emission line spectra detected at several locations of the galaxy are described in Sect 6. Concluding remarks follow in Sect 7.

2 OBSERVATIONS AND DATA ANALYSIS

2.1 Data

The data used in this work were obtained from the Multi Unit Spectroscopic Explorer (MUSE), which is an integrated field spectrograph installed in the Yepun telescope at the Very Large Telescope (VLT), Chile. MUSE covers a field of view of 1' × 1' and detects spectra in the optical region with a projected spaxel size of 0.2" × 0.2". The average seeing of the observations was ~0.78".

The data were collected on March 11, 2015 and are available on the ESO website already calibrated in flux and wavelength. The final reduced data cube has 317 by 319 spaxels and a spectral resolution from 1750 to 4650 at the wavelengths of 3750 and 9300 Å, respectively. In order to enhance the signal-to-noise ratio (SNR), in particular in regions of weak emission, a binning was performed so that each new spaxel has a final projected size of ~ 0.6"×0.6". Most of the analysis carried out in this work makes use of this rebinned cube with a size of 105 by 106 spaxels, resulting in an approximately 10.000 spaxels. When the original cube is employed, it is explicitly mentioned in the text.

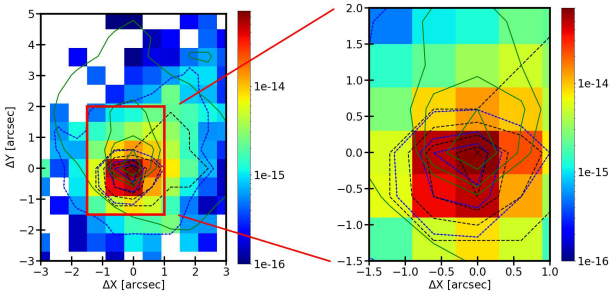

Figure 1. Left: map of [Fe X] λ6375 flux (in erg s^{-1} cm^{-2} Spaxel^{-1}) overlaid upon the contours at 7000 Å (green), [Fe XI] λ7892 (blue) and [Ar XI] λ6917 (black). Right: zoom to the innermost central region of Circinus. The symbol 'X' represents the position of the AGN.

2.2 Choice of the Circinus galaxy centre

In order to determine the precise location of the AGN, we used as a proxy the flux maps obtained for the lines of [Fe X] λ6375, [Fe XI] λ7892 and [Ar XI] λ6917 together with the continuum emission at 7000 Å, integrated within a window of 10 Å size. The choice of the above set of lines is due to their very high ionisation potential (IP > 200 eV) and by the assumption that they peak in the innermost region of the NLR, very close to the AGN. As each spaxel projects a square region of ~ 12 pc of side length, it is very unlikely that these lines peak outside the spaxel where the AGN is presumably located.

In Fig. 1, the flux distribution of [Fe X] is shown, overlaid to the contours of the continuum at 7000 Å (green), [Fe XI] (blue) and [Ar XI] (black). It can be seen that they all peak in the same spaxel. The symbol 'X' indicates the spaxel that best represents the location adopted for the AGN in the Circinus galaxy. As all our maps show relative positions, in all of them hereafter the AGN is assumed to be located at the position Δ X = 0, Δ Y = 0.

2.3 Stellar continuum subtraction

After binning the cube, we subtracted the stellar continuum. This procedure is necessary to fully recover the fluxes of the H I lines affected by the underlying stellar population. Moreover, some weak lines may also be strongly diluted by the stellar continuum. To this purpose, the stellar population synthesis code STARLIGHT (Cid Fernandes et al. 2005) was employed, together with the set of stellar populations of E-MILES (Vazdekis et al. 2016). STARLIGHT fits the continuum observed at each spaxel through the whole field-of-view of the data cube. Fig. 2 presents examples of this procedure at three different positions. Two points in the North-West region (marked as A and B) and one to the North (marked as C) of the AGN. The fitting of the stellar continuum was made in the wavelength range 3750 – 7400 Å to save computational time and to avoid regions of poor sky background subtraction that exist redwards of 7400 Å. Tests carried out by us showed that the overall fit can be affected by these residuals, while limiting the fit up to that wavelength improved the results. Redwards of 7400 Å, we use the original spectra without stellar light subtraction because that region shows very few lines that are of relevance to this work and are not even affected by the stellar component. That is the case of [S III] λ9068, located at the red edge of the spectra.

Then, we subtracted the stellar population for the entire cube in the spectral region 3750 - 7400 Å. Note that because the reso-

lution of the E-MILES and MUSE spectra are different (1 Å and 1.25 Å, respectively), we rebinnined the later to that of the former. Afterwards, we recovered the original binning of the MUSE data.

Afterwards, the extinction correction due to the Galaxy was applied. In this process, the CCM extinction law (Cardelli et al. 1989) along with an extinction value A_V of 2.1±0.4 mag, as determined by For et al. (2012), was employed.

2.4 Spectral line fit

In order to measure the flux centroid position and the full width at half maximum (FWHM) of the emission lines at each spaxel we fit Gaussian functions to individual lines or to sets of blended lines. To this purpose, a set of custom scripts written in PYTHON by our team was employed. For each line one or two Gaussian components were employed to reproduce the observed profile. Fig. 3 shows examples of the Gaussian fits carried out to the spectra at the three selected positions marked in the Hα emission line map (top left panel). It can be seen that two Gaussian component fits to each line were necessary to reproduce Hα + [N II] $\lambda\lambda$ 6549, 6583. In this process, some constraints were applied. For instance, the theoretical [N II] line flux ratio λ6583/λ6548 was used for each component. Moreover, both lines were constrained to have the same width and intrinsic wavelength separation. The [S II] $\lambda\lambda$6717, 6731 doublet was constrained to have the same width and a relative theoretical wavelength separation of 14.4 Å.

It is important to mention that at some positions (i.e., point A in Figure 3) if one single Gaussian component is fit, the RMS of the residuals is larger than when two components are employed. In order to assess if two components were indeed necessary, the code examined for a similar solution in adjacent spaxels. We are aware that the Gaussian fitting approach is a mathematical solution and the number of components necessary to reproduce a given profile is strongly related to the S/N and spectral resolution. The physical meaning of two components are always evaluated following the neighbourhood criterion. Moreover, if a component is < 3σ of the continuum RMS, that component was discarded.

Examples of Gaussian fits carried out to the [Fe VII] λ6087 line in Circinus can be found in Figure 1 of Rodríguez-Ardila & Fonseca-Faria (2020).

After measuring the fluxes of the emission lines, we determined the internal extinction affecting the gas at every spaxel. To this purpose, we used Equation 1, which makes use of the observed Hα/Hβ emission line flux ratio and the CCM extinction law. An intrinsic value of 3.1 for the above ratio was assumed and applied to the entire cube. Although we are aware of the presence of star forming regions in the field, we assumed that the AGN photoionisation dominates in the regions of interest to this work. The resulting extinction map is shown in Figure 4. In the central region (< 200 pc from the AGN) the reddening is above 1.0 mag in the East and around 0.5 mag in the West. In the outermost regions (> 200 pc away from the active nucleus) to the North-West, the reddening is rather low, with values between 0.1 and 0.4, in agreement with Mingozzi et al. (2019) results.

$$E(B-V)_{H\alpha/H_\beta} = -2.31 \times log\left(\frac{3.1}{H\alpha/H\beta}\right) \quad (1)$$

Fig. 5 displays the flux distribution of Hα (left panels) and Hβ (right panels) before and after reddening correction (top and bottom panels, respectively). The Hα emitting region is smaller after correction because the Hβ line is detected at 3σ in a region smaller than that of Hα. Only the regions displaying both lines after reddening correction are shown.

As a last step, the spectrum at every spaxel was corrected by the extinction map of Figure 5.

2.5 Gas distribution in the Circinus galaxy

In this section we will analyse the spatial distribution of the different emission lines that were found in the data cube obtained by MUSE. After the treatment of the cube (binning, subtraction of the stellar continuum, correction for Galactic and intrinsic extinction and measurement of the detected emission lines) as described in Section 2, flux maps for the most relevant emission lines identified in the different spaxels were constructed. We want to compare their spatial distribution and confirm the presence of extended emission for lines of similar or higher ionisation potential than that of [Fe VII]. In addition, we estimate the physical conditions of the coronal line region. To this purpose, it is necessary to find out suitable diagnostics to characterise the density and temperature of the high-ionisation gas.

Figure 6 presents the flux distribution of [O I] λ6300, [S II] λ6716, [N II] λ6583, [S III] λ9069, [Ar III] λ7136 and [O III] λ5007. Except for the latter line, all show a distribution similar to Hα (see Fig. 5). Moreover, they all display a prominent spiral arm that starts at the East of the nucleus towards the North, where it bends and turns to the South. Evidence of a counter arm is also observed to the South and SE of the galaxy centre. It can also be noticed that the higher the gas ionisation, the more conspicuous is the region where the ion is emitted towards the NW of the AGN. For instance, [O III] and [Ar III] map the ionisation cone more suitably than [O I].

Flux distribution maps for the high ionisation lines were also produced. Fig. 7 displays maps for He II λ5412, [Fe VII] λ6087, [Ar V] λ7006, [Fe X] λ6375, [Fe XI] λ7892 and [S XII] λ7611. For these lines, the emitting gas is extended only at the North-West and in the nuclear region. Very high ionisation lines, such as [Fe XI] and [S XII] are only detected in the nuclear region. [Fe XIV] λ5303 with IP = 361 eV (Oliva et al. 1999) is the line with the highest IP already identified in Circinus in the optical/NIR region. In this paper we report the first detection of the [S XII]λ7611 (IP = 505 eV). Its emission is not restricted to the unresolved nuclear region but it is observed up to a distance of ∼ 40 pc from the nucleus. We also report an emission line at 8340 Å in the nuclear spectrum that we tentatively attribute to [Ar XIII] λ8340 (IP = 618 eV). However, this identification is not sure as the SNR is < 3. As already mentioned, Rodríguez-Ardila & Fonseca-Faria (2020) recently reported on the detection of extended [Fe VII] emission in Circinus up to a projected distance of ∼700 pc from the AGN. Here, we also found extended [Fe X] λ6374 emission on scale of hundreds pc. In the nuclear and circumnuclear region, the gas emitting this line shows a clearly elongated morphology in the NW-SE direction, nearly coinciding with the radio jet axis and extending up to 140 pc from the centre. Beyond it, the line fades below the detection limit. It reappears at ∼280 pc from the AGN in the same direction as the circumnuclear extended region forming an extended cloud of several tens of pc size that is clearly resolved by MUSE and it is visible up to ∼350 pc from the nucleus. The region where the extended [Fe X] emission is observed coincides in position with the brightest part of the extended Fe^{+6} gas. To the best of our knowledge, this is the first time that extended Fe^{+9} gas at such distance scales is reported in a radio-quiet AGN.

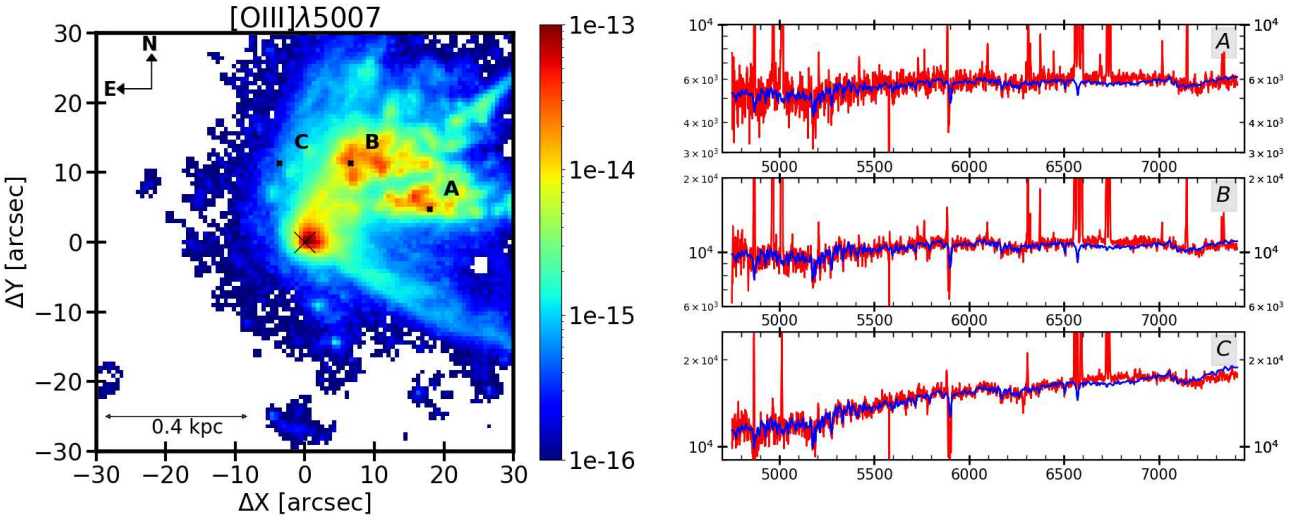

Figure 2. Left: map of the emission line flux for [O III] λ5007 (in erg s^{-1} cm^{-2} Spaxel^{-1}). Right: examples of the continuum fit by STARLIGHT at the three selected positions indicated in the map of [O III]λ5007 flux (in 10^{-20} erg s^{-1} cm^{-2} Å^{-1}). A and B are in the extended North-West region of the ionisation cone. C is in a region dominated by the galaxy disc. The observed spectrum is in red and the best fitting stellar population models are in blue. The black cross in the left panel marks the position of the AGN. White areas correspond to spaxels that were masked because the S/N <3.

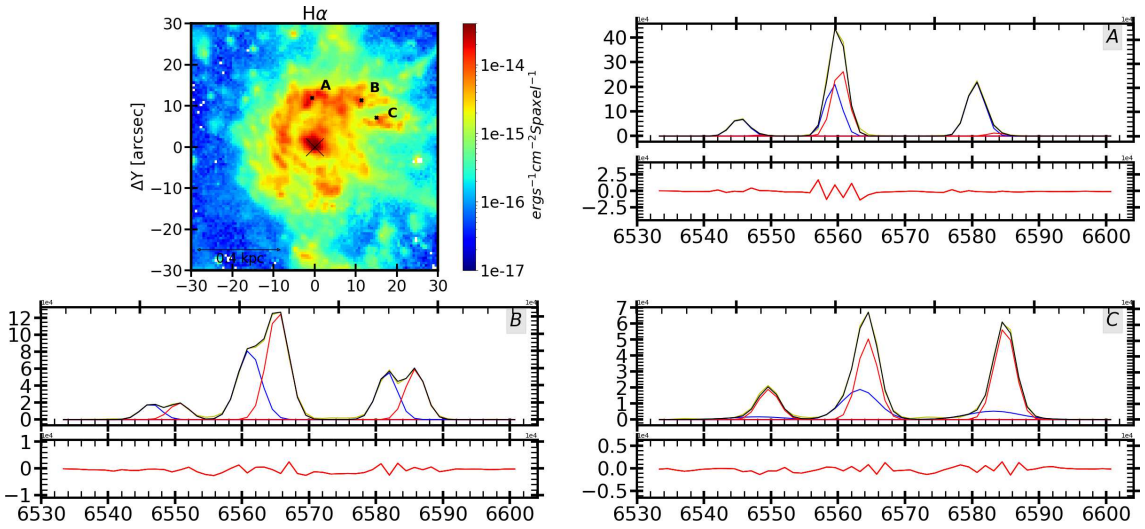

Figure 3. Top left: flux map of Hα. The black cross indicates the AGN position. Panels marked as A, B, and C show examples of the Gaussian fits carried out to the Hα+[N II] $\lambda\lambda$ 6549, 6584 lines at some selected positions, identified in the Hα map. In the example fits, the Y-axis scale is in units of 10^{-16} erg s^{-1} cm^{-2} Å^{-1} and the X-axis is the wavelength in Angstroms. The blue and red Gaussian components are shown with their respective colour. The residuals of the fit are shown in the bottom boxes. The black line represents the observed spectrum.

2.6 Distribution of emission line flux ratios

We use the emission-line fluxes shown in the preceding section to construct line intensity-ratio maps. The main goal is to investigate how the different distributions of the line flux ratios to Hβ behave. The results are shown in Fig. 8. In all the maps, the lines are reddening corrected.

Interestingly, Fig. 8 shows that most of the high-ionisation line ratios to Hβ are enhanced in the extended [Fe VII] region. Moreover, the ratios of these lines increase with increasing distance from the AGN. For example, [Fe VII]/Hβ has values of $\sim 10^{-2}$ at 240 pc from the AGN while at 700 pc it is nearly an order of magnitude larger ($\sim 10^{-1}$). A similar behaviour is observed for [O III] and [Ar V], where an increase by a factor of $\sim$ 5 in the line flux ratio to Hβ is found outwards. Low-ionisation lines are weak relative to Hβ in the region dominated by the extended [Fe VII]. They become stronger outside the region filled with the high-ionisation gas.

The peculiar extended gas distribution e.g. the increase of the [Fe VII]/Hβ ratio cannot be easily explained by the central source photoionisation alone.

3 PHYSICAL CONDITIONS OF THE GAS

In order to get clues about the processes that power the strong high-ionisation outflow detected in Circinus (Rodríguez-Ardila & Fonseca-Faria 2020), we determine the electron temperature, T_e and density, n_e in the regions co-spatial

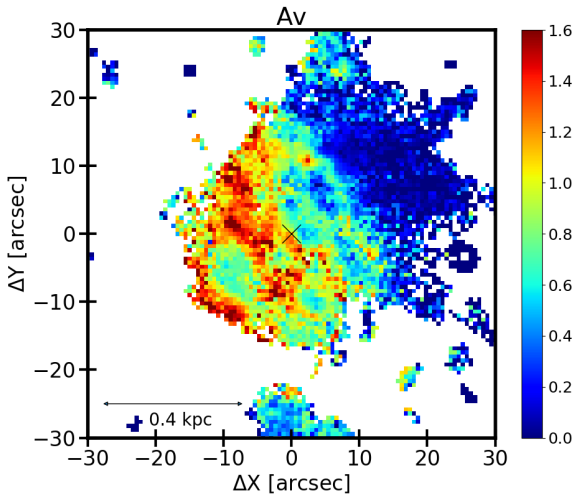

Figure 4. Intrinsic extinction map derived for Circinus. The symbol 'X' indicates the AGN position as determined in 2. White areas correspond to masked regions where the S/N < 3.

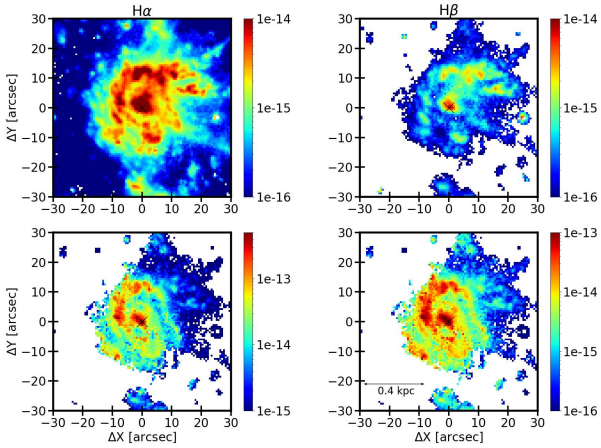

Figure 5. Flux maps for Hα (left panels) and Hβ (right panels) before (top) and after (bottom) reddening correction. The colour bar is in units of erg s^{-1} cm^{-2} Spaxel^{-1}. White areas correspond to mask values of SNR <3. The black cross indicates the AGN position.

to the [Fe VII] λ6087 emission. T_e in each spaxel was derived from the [S III] line ratios by means of Equation 2 (Osterbrock & Ferland 2006). MUSE has a wavelength cutoff at 9200 Å, so that at the redshift of Circinus, the [S III]λ9069 Å is observed. Using the intrinsic ratio determined from quantum mechanics, [S III] λ9532 = 2.44 × [S III] λ9069 and Eq. 2, it is possible to employ the S^{+2} ions for temperature diagnostics. Fig. 9 shows the results obtained for the regions where the lines of [S III] have a SNR > 3. In this calculation, a n_e = 400 cm^{-3} was employed. Electron densities were evaluated from the [S II] line ratios (see below). Increasing or decreasing the gas density by a factor of 2 has negligible effects on the gas temperature. The [S III] λ6312 line is at least a factor of 10 weaker than [S III] λ9069. T_e was evaluated in the spaxels where all three lines have SNR >3. Thus, the electron temperature was effectively determined at just a few particular regions of the MUSE detector. Note that [S III] λ6312 was mostly detected in the same spaxels where the bulk of [Fe VII] is observed.

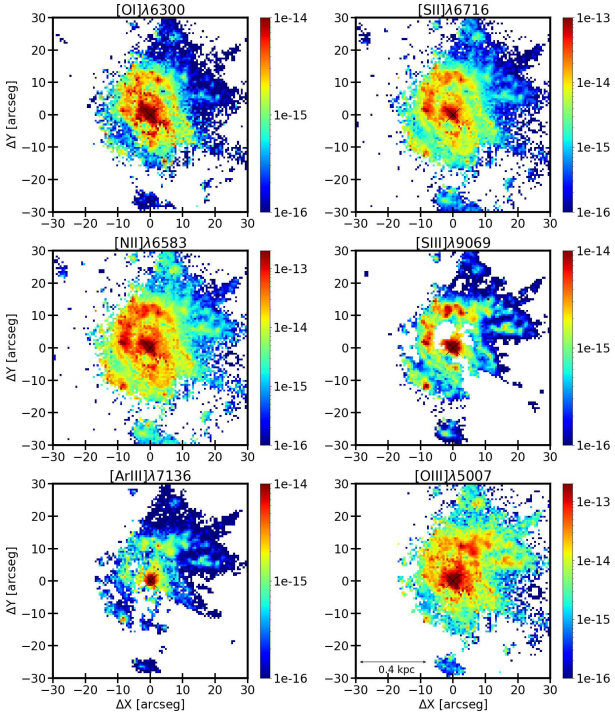

Figure 6. Emission line flux distribution for [O I]λ6300, [S II]λ6716, [N II]λ6583, [S III]λ9069, [Ar III]λ7136 and [O III]λ5007. The colour bar is in units of erg s^{-1} cm^{-2} Spaxel^{-1}. North is up and East to the left.

Therefore, on a first approximation, T_e determined above can be representative of the coronal iron line emission gas if we consider that [S III] and [Fe VII] emitting clouds are co-spatial. Fig. 9 shows the temperature distribution derived from the [S III] line ratio. In the region where [S III] λ6012 is detected, all the sulphur lines display a double-peaked profile. Thus, we determined T_e for the blue and red components separately. The values found for the blue component is nearly twice as high as those of the red component. In particular, there is a hot spot where T_e reaches 3×10^4 K while in most other regions T_e is ~ 1.5×10^4 K. In some spaxels, Equation 2 converges to non-physical values. In these cases, the values were masked from Fig. 9.

$$[\mathrm{S\,III}]\frac{j_{\lambda9532}+j_{\lambda9069}}{j_{\lambda6312}} = \frac{5.44\times exp(2.28\times10^4/T)}{1+3.5\times10^{-4}\times n_e/T^{1/2}} \quad (2)$$

Rodríguez-Ardila & Fonseca-Faria (2020) proposed a scenario suitable to explain the gas morphology seen in Fig. 9 consisting in an expanding bubble produced by the passage of a radio jet. For both [S III] and [Fe VII] lines, the flux distribution are similar, most likely co-spatial. This can be noticed by the excellent correspondence between high temperature and high ionisation line represented by the [Fe VII] λ6087 emission.

We obtain n_e in each spaxel from the [S II] λ6716 / λ6732 line ratio along with Equation 3 assuming T_e = 1.5 × 10^4 K. This value is consistent with the T_e previously determined in Circinus. Equation 3 was derived by Proxauf et al. (2014) and represents a correction to the one found by Osterbrock & Ferland (2006). For the density determination we followed two approaches. First, we used the sum of the blue and red components because at some locations the lines were double-peaked while in others a single component was found. Second, we determined the density for each component

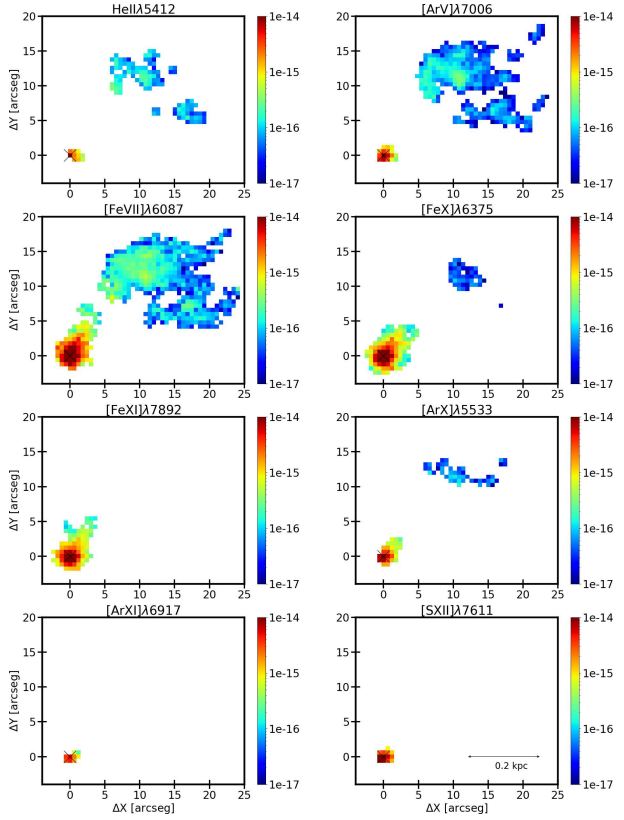

Figure 7. Flux map distribution for He IIλ5412, [Ar V]λ7006, [Fe VII]λ6087, [Fe X]λ6375, [Fe XI]λ7892, [Ar X]λ5533, [Ar XI]λ6917 and [S XIII]λ7611 in units of erg s^{-1} cm^{-2} Spaxel^{-1}. On each panel, the cross marks the position of the AGN. Only the NW quadrant of the MUSE detector is shown because the extended, high-ionisation emission is located entirely in the nuclear region and to the NW.

separately for the gas located in the NW region where the sulphur lines are double-peaked.

$$log(n_e[cm^{-3}]) = 0.0543 \tan(-3.0553R + 2.8506) + 6.98 - 10.6905R + 9.9186R^2 - 3.5442R^3 \quad (3)$$

where R is the line flux ratio [S II] λ6716/λ6732.

Fig. 10 shows the electron density in Circinus derived from the sum of the blue and red components of the [S II] lines (top panel) and the density determined separately for the blue and red components (bottom panels). Notice that in this calculation, only sulphur lines with $S/N > 5$ were employed. The results show two main regions of high density, one at the location of the AGN, and the other in the NW side of ionisation cone, the same region where the [Fe VII] λ6087 gas is observed. A gas density of $n_e > 400$ cm^{-3} is found in that region. Interestingly, it coincides with the region of the highest temperature derived previously, which could be interpreted as another indication of a shocked gas.

4 STELLAR AND IONISED GAS KINEMATICS

The study of the gas kinematics in a galaxy is an important tool to separate the contribution of the main stellar disc component from other contributions such as a bar, an ionisation cone or a circumnuclear disc. It also allows to identify inflowing/outflowing components and their relationship with a possible radio jet. In the case of the Circinus galaxy, disentangling the different kinematic components is fundamental because of the strong contribution of the host galaxy. To isolate the different components, we will first determine the stellar kinematics and afterwards, the gas kinematics.

4.1 Stellar kinematics

We modelled the kinematics of the Circinus host galaxy using a rotation model given by Equation 4. It was proposed by Bertola et al. (1991) in order to fit the line of sight velocity of a rotation disc. To derive the parameters which best represent the stellar component, the Ca IIλ8662 absorption line was employed.

$$v_{mod}(R,\Psi) = v_{sys} + \frac{AR\cos(\Psi-\Psi_0)\sin\theta\cos^p\theta}{\left\{R^2[\sin^2(\Psi-\Psi_0)+\cos^2\theta\cos^2(\Psi-\Psi_0)]+c_0^2\cos^2\theta\right\}^{p/2}} \quad (4)$$

In Equation 4 v_{mod} is the line of sight velocity, v_{sys} is the systemic velocity of the galaxy, A is the amplitude of the velocity, Ψ_0 is the angular position of the nodes, i is the slope of the disk in relation to the sky plane, c_0 is the concentration parameter defined as the radius where the curve has 70 percent of the maximum rotational velocity and p measures the flatness of a curve of the galaxy. This last parameter can be between 1 and 1.5 for external regions of the galaxy. When $p = 1$ the rotation curve at large radii is asymptotically flat and for $p = 1.5$ it has a finite mass. R is the radial distance to the nucleus and Ψ is the angle where the radius R is measured in the sky plane.

The observed position-velocity map derived for the Ca II absorption line is shown in the top left panel of Fig. 11. The top right panel of that figure presents the best model fit by Equation 4. In this process, the following parameters were obtained: $v_{sys} = 21.2 \pm 0.2$ km s^{-1} (the actual adjusted systemic velocity is 455.3 km s^{-1} and a systemic velocity correction of 434.1 km s^{-1} Meyer et al. (2004) was adopted), $a = 715 \pm 50$ km s^{-1}, $\Psi_0 = 289.6° \pm 0.2$, $i = 50.3° \pm 0.5°$, $c_0 = 7.1'' \pm 0.2$ and $p = 1.61 \pm 0.02$. The bottom panel of Fig. 11 displays the residuals obtained after subtraction from the observed position-velocity diagram the best fit model. In general, the residuals are very close to zero everywhere but at some positions (mostly to the SW), where residual velocities smaller than 50 km s^{-1} are found. Overall, our results imply that the stellar component is best described in terms of a stellar disc, that we interpreted as the galaxy disc.

4.2 Emission gas kinematics

The rotation model expressed by Equation 4 was also applied to the emission-line gas using the narrow component of Hα. This choice is because we associated it mostly to the rotating gas disc. The second component fit to the Hα line is usually broader and likely associated to outflowing gas. In Fig. 12, the observed position-velocity (PV) maps derived for the narrow (left) and broad (right) components of Hα are shown in the two top panels. The central panel in the second row presents the best fit to the PV map of the Hα narrow component. The following parameters were obtained: $v_{sys} = 0.6 \pm 0.7$ km s^{-1} (the actual fit systemic velocity is 434.7 km s^{-1}), $a = 246.2 \pm 4.5$ km s^{-1}, $\Psi_0 = 287.6° \pm 0.4$, $i = 60.8° \pm 1.2°$ and $c_0 = 17.3'' \pm 1.0$. We fixed $p = 1.0$. The bottom panels of Fig. 12 show the residuals obtained after subtracting the

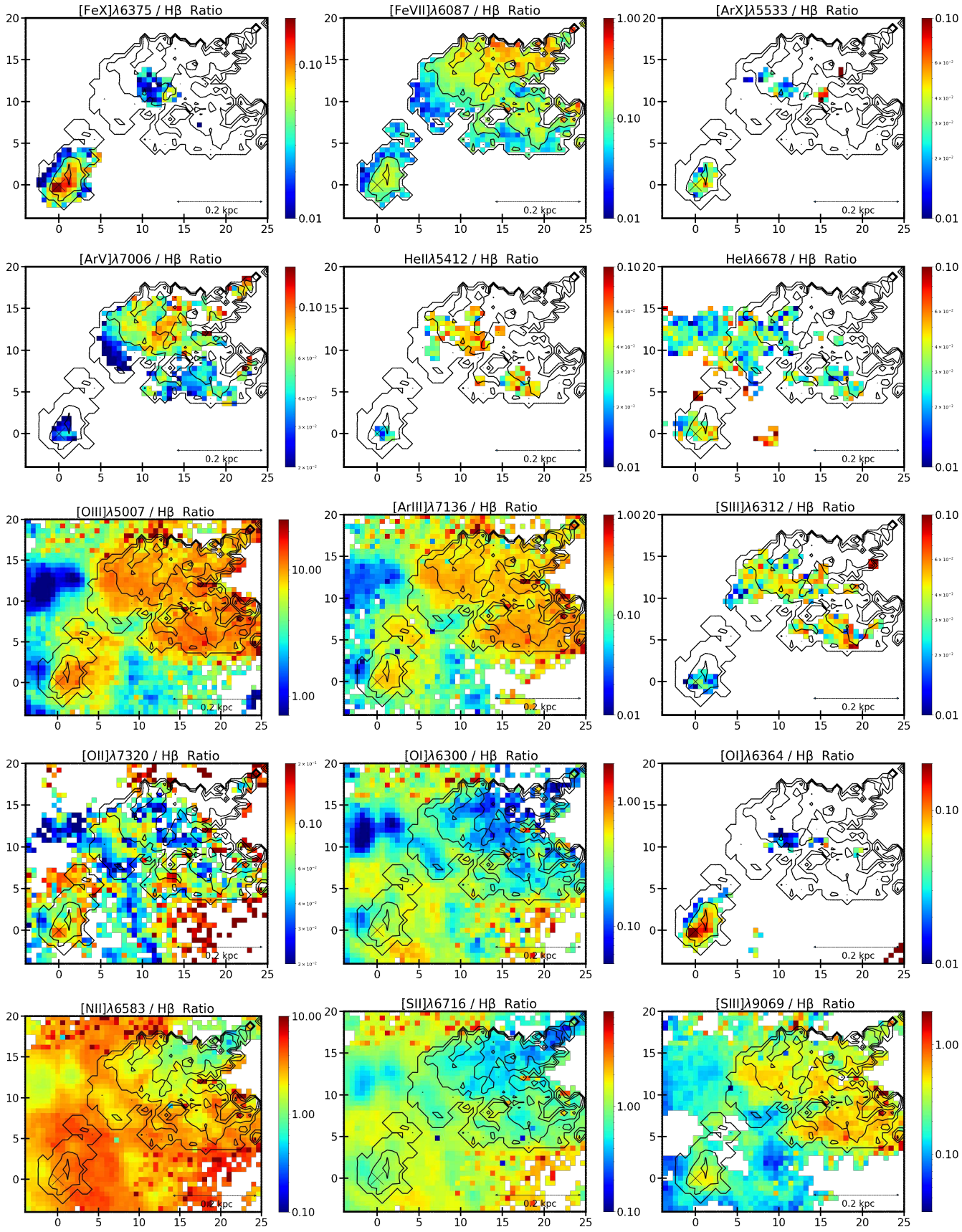

Figure 8. Emission line flux ratios for the most prominent ions detected in the spectra of Circinus. In all panels, the black contours represent the ratio of [Fe VII]/Hβ with levels of 0.001, 0.08 and 0.17. The white regions correspond to locations where the lines where not detected.

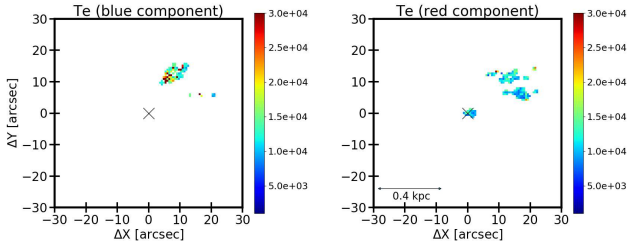

Figure 9. Temperature distribution for the blue and red components (left and right panels, respectively) obtained from the [S III] lines. The colour bar is in units of Kelvins. (see Sect. 3).

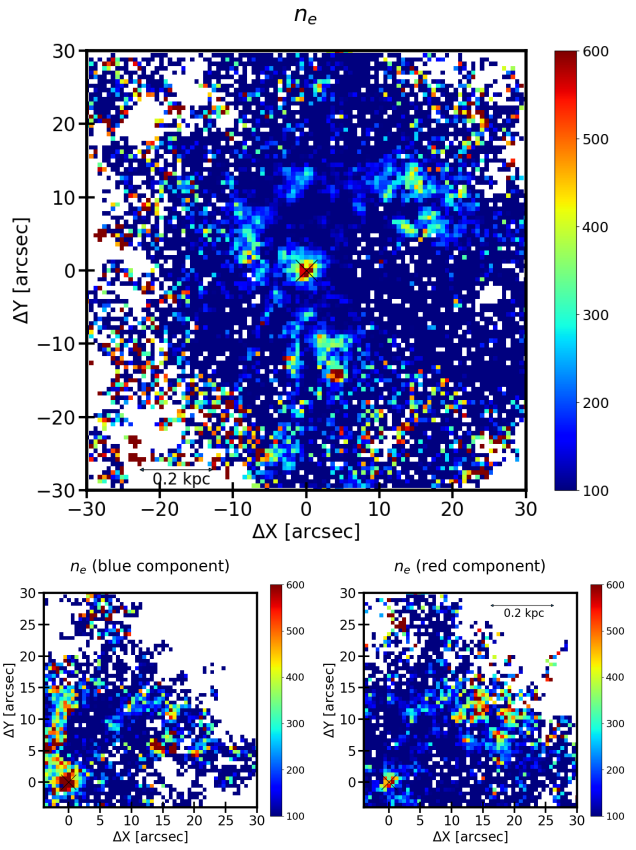

Figure 10. Density maps (in cm^{-3}) obtained from the [S II] lines. Top panel: density determined using the sum of the blue and red components of the lines. Bottom panels: n_e found for the blue (left) and red component (right) fit to each of the two sulphur lines.

best model to the observed PV diagrams of the narrow and broad components. It can be seen that the narrow component of Hα suitably describes the ionised gas rotation in the the galaxy disc. Departures from the rotation model are observed in the Northwest region, with velocity values in excess of up to 200 km s^{-1}. We attribute this discrepancy to the fact that part of the gas in this region is out of the galaxy plane, in the ionisation cone, so that the observed emission is a contribution of both the galaxy disc and outflowing material. As expected, the broad component, which best describes the ionised gas outflow, has residuals of order of 100 km s^{-1} in absolute value in most locations where it is observed.

Elmouttie et al. (1998) previously studied the ionised gas in Circinus obtaining a rotation axis of 292°, an inclination angle of

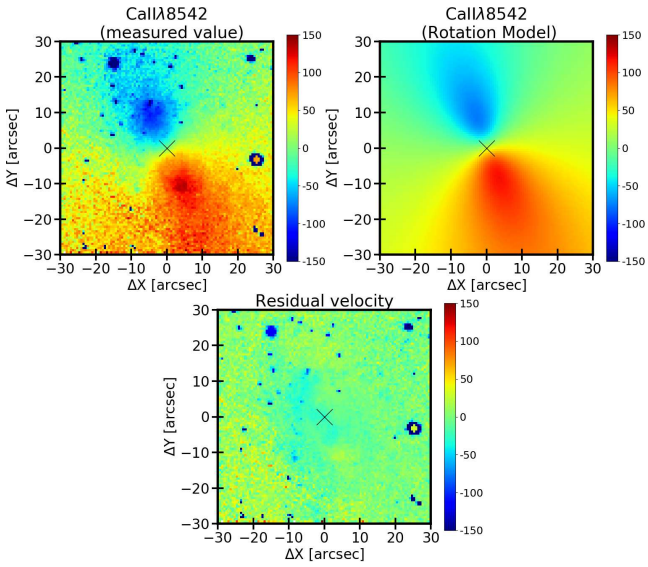

Figure 11. Position-velocity diagram measured for the Ca II line (top left). The best fit model is in the top right panel. Residuals, after subtraction of the best fit model to the data is in the bottom panel. The colour bar is in units of km s^{-1}.

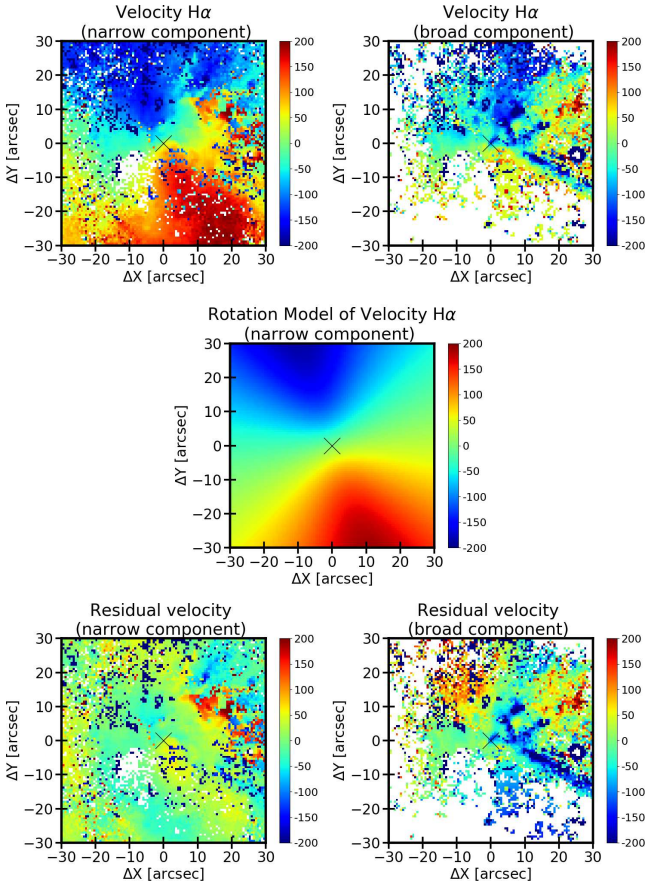

Figure 12. Position-velocity map for the narrow (top left) and broad (top right) components of Hα. The best model for the narrow component is shown in the central panel. The two bottom panels show the residuals left after subtraction of the best fit model to the observed data for narrow (left) and broad (right) components. The colour bar is in units of km s^{-1}.

40° ± 10°, and a rotation velocity of 350 km s^{-1}. It can be seen that the most important parameters agree very well within errors. The difference between the value of the inclination angle obtained by Elmouttie et al. (1998) data and ours is mainly due to the size of the field (in their work it is about 30" × 30" arcsec). They also show that the host galaxy is moderately inclined relative to the observer. Due to its proximity, the host should appear in foreground to the gas emission.

4.3 Channel maps for Hα and [O III] lines

We have also studied the gas kinematics using channel maps extracted from the Hα and [O III] emission line profiles. To this aim we use the MUSE cube with the original binning in order to preserve the best possible angular sampling (spaxel size of 0.2"). The procedures described in Sect. 2 for processing the binned cube (i.e. stellar continuum subtraction and extinction correction) were also applied to the original cube. Figs. 13 and 14 show channel maps for the Hα and [O III], respectively, both in bins of $\Delta\lambda$ = 1.25 Å. Regions where the measured flux is less than $1.5\times\sigma_{sky}$ have been removed from the maps and appear in white. σ_{sky} is the standard deviation of the sky noise.

We found that for Hα the most extended emission features within the NW ionisation cone display velocities between -375 km s^{-1} and 422 km s^{-1}. Moreover, filaments and several emission knots associated to them are evident in the channel maps. The most conspicuous filament is seen in the velocity channels -204 km s^{-1}, -147 km s^{-1} and -90 km s^{-1}. It runs from the AGN to the SW and it is usually identified with the Southern edge of the ionisation cone. There is also a filament in the velocity channels -33 km s^{-1} and 23 km s^{-1}, which seems to arise in the galaxy nucleus and it is projected towards the NW at a PA of ∼ 305°. We have clearly identified 14 knots of Hα emission in the channel maps, marked with black circles in both figures. These knots are better seen in the velocity channels -90 km s^{-1}, -33 km s^{-1}, 23 km s^{-1} and 80 km s^{-1}, although some of them appear in the channel maps corresponding to velocities of -375 km s^{-1} and 422 km s^{-1}. The same knots are also detected in [O III], as can be seen in Fig. 14. Moreover, they show up with larger projected blueshifted velocities, being detected at -675 km s^{-1} relative to the systemic velocity. The connection with the filaments is even more evident here, mainly at the centre and at the edges of the cone. The filamentary structure in the ionisation cone already noticed in Hα is enhanced in [O III], with at least six filaments of emission detected in the channel maps, in particular for velocities corresponding to -2 km s^{-1} and 71 km s^{-1}. Some of the filaments and knots we found in Circinus were already presented by Veilleux & Bland-Hawthorn (1997). These authors report that one of these filaments, the one that runs from the nucleus to the West, extends up to 40" (∼ 800 pc). Fig. 14 shows that this same filament is detected here, up to the West edge of the MUSE detector. Moreover, the filament closely aligned with the radio jet axis is observed up to a distance of ∼1 kpc from the AGN.

The excellent sensitivity achieved with MUSE also allows us to detect a larger number of knots, called "bullets" by Veilleux & Bland-Hawthorn (1997). They identified four main bullets at ∼11", 18", 30" and 37" from the AGN with a PA ∼270° from the nucleus. In addition, we identified other systems of bullets at distances smaller than 10" from the AGN. Veilleux & Bland-Hawthorn (1997) argue that the motions observed across the ionisation cone are highly supersonic, therefore high-velocity (V$_s$ > 100 km s^{-1}) shocks are likely to contribute to the ionisation of the line-emitting gas. Additional support for this

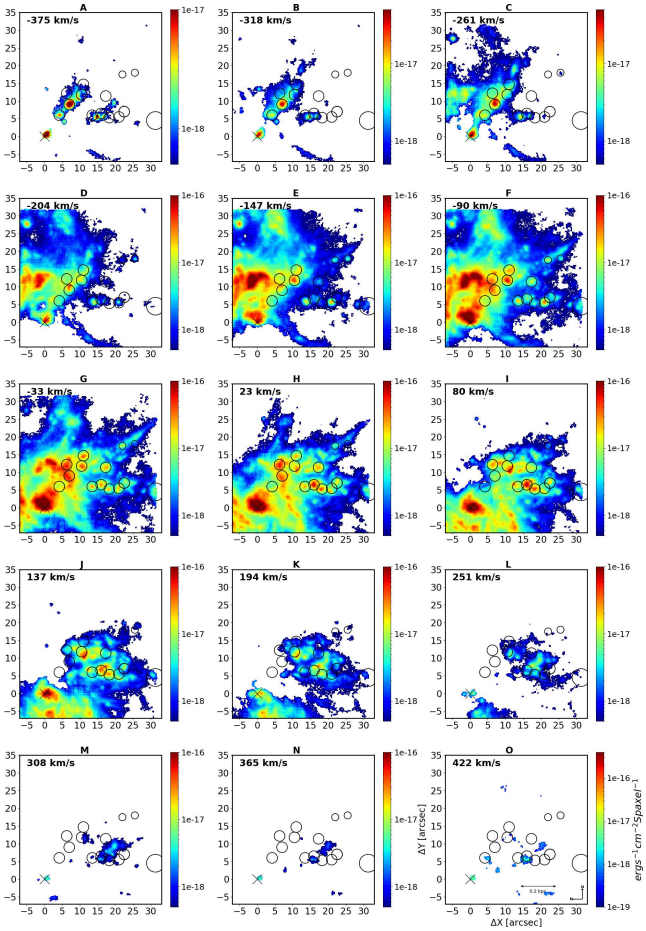

Figure 13. Channel maps along the Hα emission-line profile, in order of increasing velocities, shown in the upper left corner of each panel. The black, open circles, mark the position of knots of emission, identified in the maps. The flux is indicated by the colour bar, in units of erg s^{-1} cm^{-2} spaxel^{-1}.

scenario comes from the detection of high-ionisation emission on large scales filling up the region where most of the bullets are located. The velocity field of the knots and their strong association with the filaments suggest that they represent material either expelled from the nucleus or dragged by a wide-angle wind aligned to the polar axis of the galaxy. The current radio data available for Circinus support that the wide-angle wind is jet-driven. Indeed, the northwest ionisation cone appears to have a radio counterpart at both 13 and 20 cm (figs. 5 and 6 of Elmouttie et al. 1998). This conclusion is drawn from the comparison between Figs. 13 and 14 and their radio maps.

4.4 Moment maps for the low and medium ionisation lines

In order to further characterise the kinematics of the ionised gas in Circinus, we constructed moment maps (flux, velocity, FWHM) for the most prominent emission lines detected in the galaxy. Fig. 15 displays the results for Hα, [O I] λ6300, [S II] λ6716 and [N II] λ6583. At some positions (i.e. within the ionisation cone), each of the above lines were fit using two Gaussian components while at others, one component was enough to fully represent the observed profile. For the sake of clarity, we present maps for the two components, separately. When only one component is observed, the line appears either as a blue or as a red component.

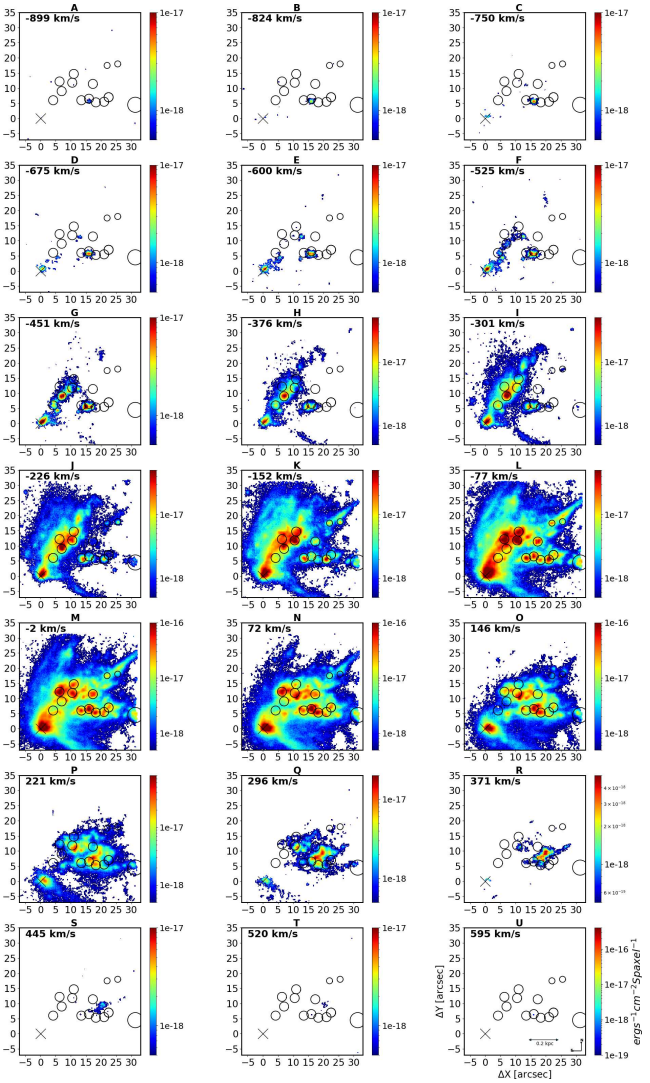

Figure 14. Same as Figure 13 but now for the [O III] emission-line profile.

The flux maps displayed in the first column of Fig. 15 show that the low-ionisation lines are particularly enhanced in the nuclear and circumnuclear region of the galaxy (central 10" × 10" around the AGN). They nicely trace the prominent ring of star formation that characterises Circinus, previously reported and studied by other authors (Marconi et al. 1994; Curran et al. 1998). Moreover, the low-ionisation gas is also clearly extended towards the NW, within the ionisation cone. It fills all the FoV covered by the detector both towards the North and West sides of the galaxy. Some extended emission is also detected towards the South but it is not possible to state so far whether it is located in the counter-cone or in the galaxy disc. Anyway, the emission line flux in the cone and Southern part is weak, nearly two to three orders of magnitude fainter than in the central regions of the galaxy. From the position-velocity diagrams in Fig. 15 (central panels) we found that in most parts of the galaxy, the low-ionisation gas is in rotation, similar to what is observed in Hα, except in the NW side, where the gas is largely out of the galaxy plane. This region spatially coincides with the high-ionisation component of the outflow. A long radial filament of gas, with velocities between -200 km s^{-1} and -100 km s^{-1}, is also evident towards the SW, mainly from the blue component of the lines. We associate this feature to the SW edge of the ionisation cone, already noticed by Mingozzi et al. (2019). This filament is also characterised by a larger velocity dispersion, particularly seen in the [N II] and [S II] lines. The FWHM reaches values larger than 300 km s^{-1}, similar to the widths found in the central part of the ionisation cone. Fig. 16 shows moment maps for the blue and red components of the mid-ionisation lines [O III] λ5007, He II λ5412, [Ar III] λ7136 and [S III] λ9069. As for the low-ionisation emission discussed above, the prominent starburst ring is also enhanced by these lines except He II. This latter emission is only detected at the AGN position and in the highest ionised portion of the NW cone.

There is also some evidence that part of the gas emitting [O III], [Ar III] and [S III] is located in the galaxy disc. This result is gathered from the detection of blue- and red-shifted emission following the rotation pattern found in Hα. Moreover, towards the Northwest, the outflow component is evident and highlighted by the mid-ionisation emission. A wide range of velocities is also detected by the mid-ionisation gas (see central panel of Figure 11) which displays a larger width to the Northwest (FWHM > 300 km s^{-1}) and gas velocities which strongly deviate from rotation, confirming that most of the gas in the ionisation cone is out of the galaxy plane.

4.5 Moment maps for high ionisation lines

We also study the kinematics of the most important high ionisation lines detected in Circinus in the wavelength range covered by the MUSE data (3750 to 9300 Å). In Figure 17 we present the moment maps of the blue and red components of [Fe VII] λ6087 and [Ar V] λ7006 and in Figure 18 the moments for [Fe X] λ6375. It is evident from Figures 17 and 18 that, in contrast to the low- and mid-ionisation lines, coronal lines although extended are observed only in two regions: in the nucleus and in the highest ionised portion of the NW cone. Indeed, no evidence of such lines are found in the cone edges, as seen in e.g. Hα or [O III]. Notice that [Fe X] is also detected in the cone but at two very specific locations. In none of the three coronal lines considered here evidence of gas rotation is observed, confirming previous results derived from the low- and mid-ionisation lines, that the bulk of the ionised gas in the cone is out of the galaxy plane. The detection of split line profiles at most positions in the central part of the ionisation cone further supports this scenario. The data suggest an expanding bubble of gas with the approaching and receding maximum velocities reaching nearly -300 km s^{-1} and 200 km s^{-1}, respectively.

The [Ar V] emission (Figure 17) shows a flux distribution very similar to that of [Fe VII] but restricted to a more compact region. The [Fe X] line (see Figure 18) was detected in the nucleus and up to ~40 pc towards the NW. Moreover, to the best of our knowledge, we detected, for the first time in the literature, [Fe X] emission at a distance of 340 pc from the AGN. The emission is produced by a cloud with a diameter of 60 pc, best traced by the red component of the [Fe X] line profile. It agrees in velocity, FWHM and spatial position with the most intense emission detected in [Fe VII].

4.6 A 3D kinematic model for Circinus

Two main results about the kinematics of the coronal gas were derived in previous sections. First, the coronal gas is out of the galaxy plane with most of that emission taking place in the central region of the ionisation cone. Second, the gas is clearly in expansion with two main components. The northern portion is outflowing towards the observer while the bulk of southern component is receding from us. 3D projection modelling of this scenario is presented in Figure 19 for the velocity components of [Fe VII]. The left

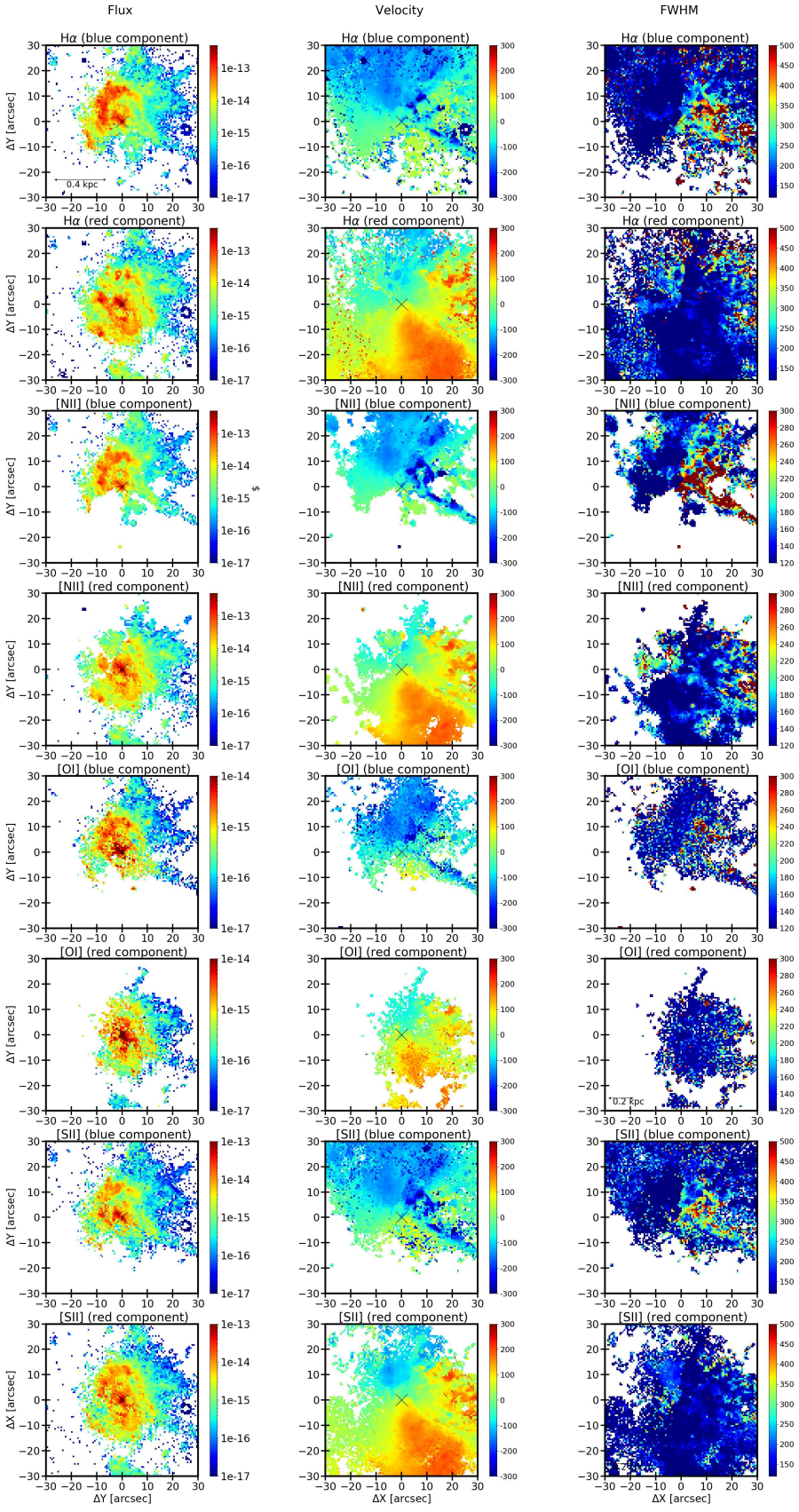

Figure 15. Moment maps for the low ionisation lines Hα, [O I]λ6300, [S II]λ6716 and [N II]λ6583. Flux scale is in units of erg s^{-1} cm^{-2} Spaxel^{-1}. Velocity and FWHM are in units of km s^{-1}.

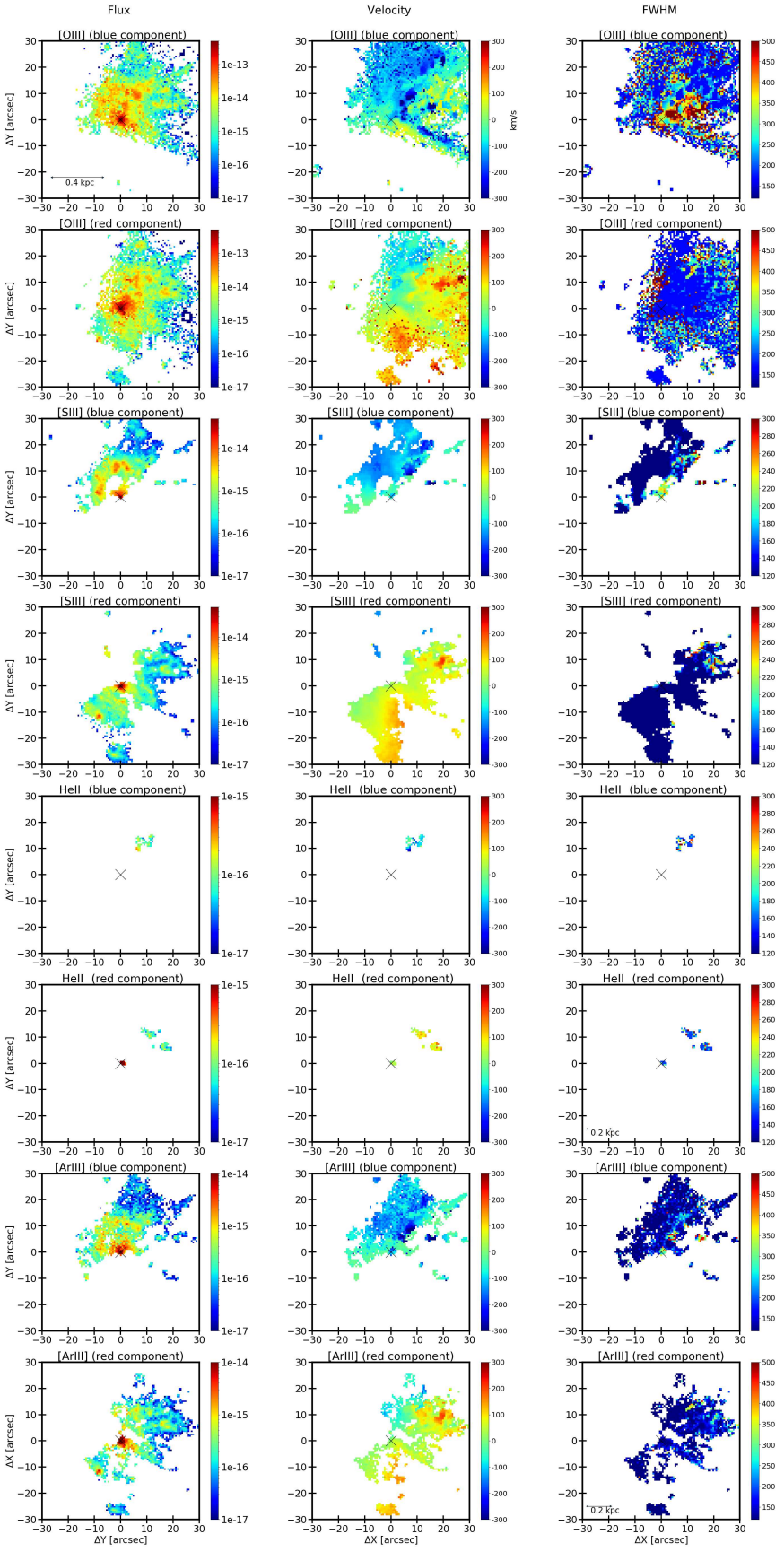

Figure 16. Moment maps for mid-ionisation lines: [O III]λ5007, [S III]λ9069, [HeII]λ5412 and [Ar III]λ7136. Flux scale is in units of erg s^{-1} cm^{-2} Spaxel^{-1}. Velocity and FWHM are in units of km s^{-1}.

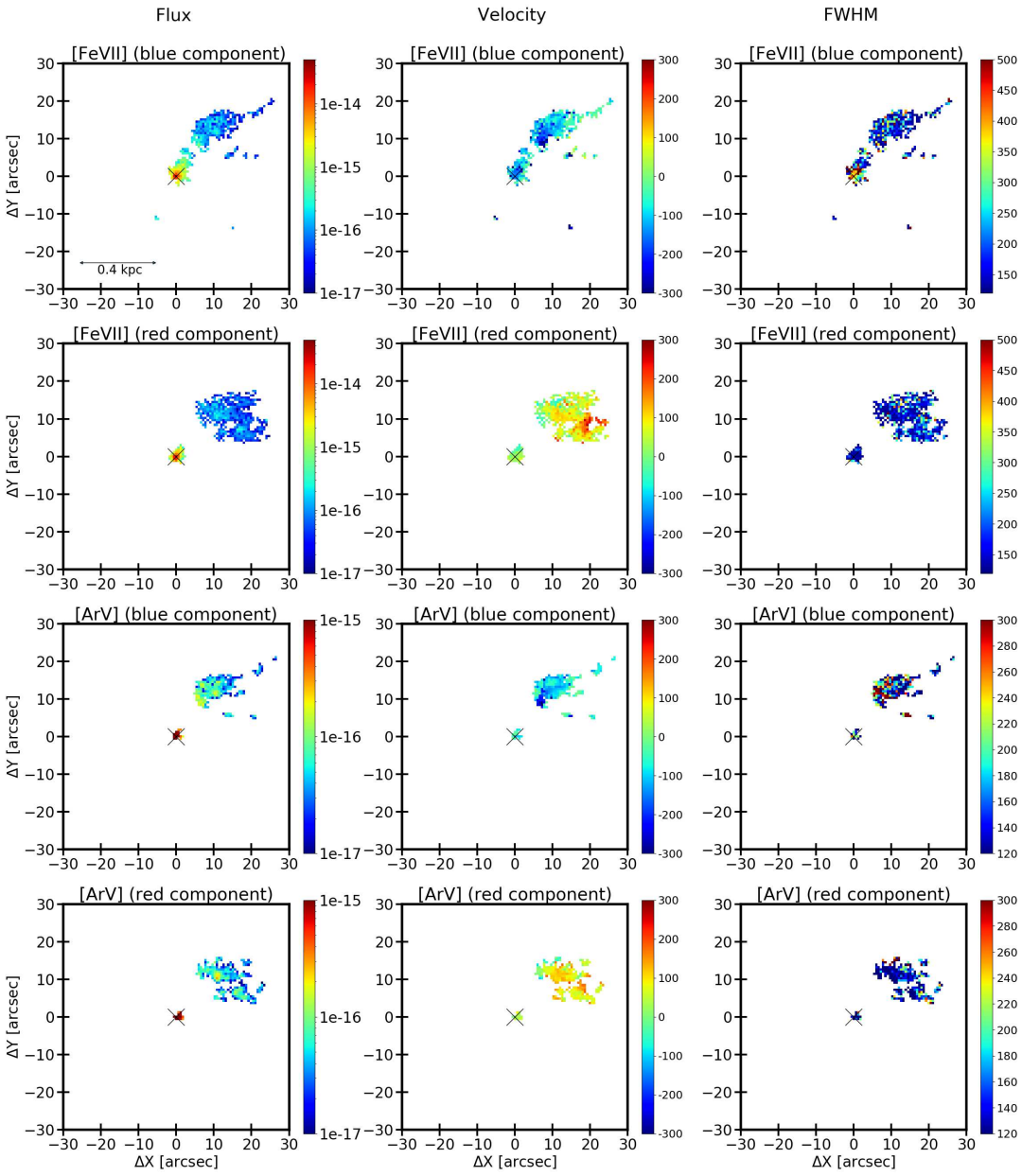

Figure 17. Moment maps for the high ionisation lines [Fe VII]λ6087 and [Ar V]λ7006. Flux scale is in units of erg s^{-1} cm^{-2} Spaxel^{-1}. Velocity and FWHM are in units of km s^{-1}.

panel depicts the ΔX and ΔY axes which define the two spatial dimensions. The z-axis shows the gas velocity component. Negative values are coloured in blue while positive ones are in red. Notice that this model resembles the current gas morphology observed, for instance, in Figure 17. The panel to the right is equivalent to the left panel after applying a clockwise rotation of ~90^{o} to the XY plane and untilting the velocity axis. It can be seen that the gas velocity field suggests an expanding cocoon. We speculate that this feature could be formed by the passage of a radio jet which, since then, is expanding freely out of the galaxy plane. The left panel of Figure 20 shows the rotation model fit to the galaxy disc overlaid upon the velocity components of [Fe VII]. The right panel shows the rotation model derived for Hα. The blue dots indicate negative velocities while the red dots positive velocities. It can be clearly seen that the [Fe VII] gas is detached from the rotation of the galaxy disc.

4.7 Velocity-velocity dispersion diagram

The gas kinematics can also be studied by means of the so-called velocity versus velocity dispersion (VVD) diagram (i.e., Karouzos et al. 2016; Woo et al. 2016). It allows us to investigate if the observed velocity shifts and velocity dispersion are related. Figure 21 presents the VVD diagram for the narrow (black circles) and broad (red circles) components of the [O III] line measured in the ionisation cone of Circinus. The grey horizontal area indicates the stellar velocity dispersion, σ_*, measured along the galaxy disc

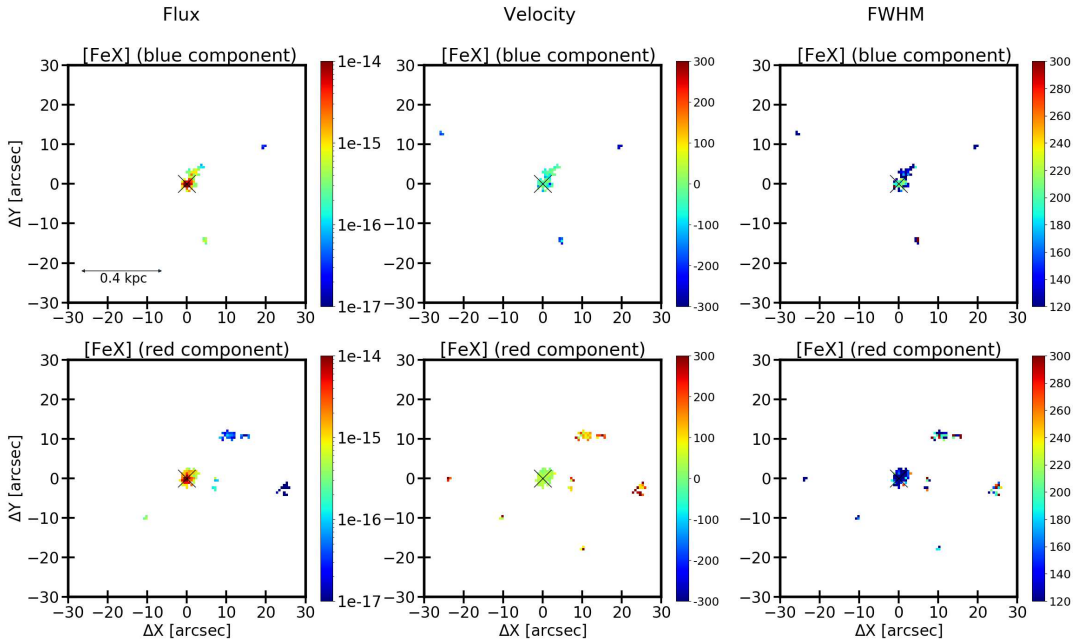

Figure 18. Moment maps for the high ionisation line [Fe x]λ6375. Flux scale is in units of erg s^{-1} cm^{-2} Spaxel^{-1}. Velocity and FWHM are in units of km s^{-1}.

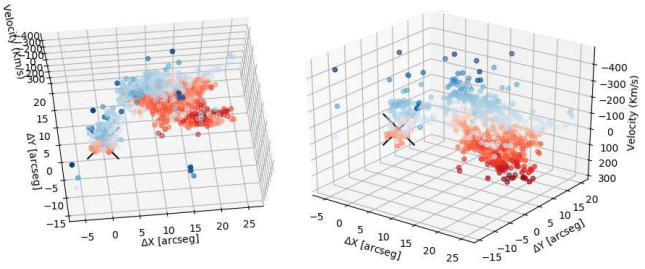

Figure 19. Velocity maps of the [Fe VII]λ6087 line (left) on the XY plane (similar to Figure 17) and (right) by a different angle of view. The centre of the galaxy is represented in black.

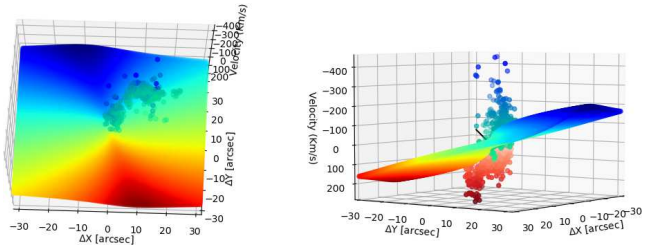

Figure 20. Rotation model in a 3d map already presented in section 4. Left: the rotation model for the Hα line. The blue dots indicate the velocity for the [Fe VII]λ6087 component. Right: rotation model together with the blue and red speed components of [Fe VII].

by means of the CaT lines. The V=0 km s^{-1} represents the systemic velocity of the galaxy.

Several interesting results can be observed in Figure 21. First, there is a clear difference between the kinematics of the broad and narrow components. The former shows larger velocity dispersion, with values of up to 260 km s^{-1} and larger velocity offsets, with blueshifts reaching −400 km s^{-1} . In contrast, in the latter the velocity dispersion is restricted to the σ_* values of the galaxy. Second, the VVD diagram of the narrow component shows two distinct distributions: one clustered at −40 km s^{-1} and another at −120 km s^{-1} . As all the points shown refer to the NW portion of the ionisation cone, we discard that the separation is due to the galaxy rotation. Moreover, the two clustered velocities are not distributed evenly along V=0 km s^{-1} but systematically shifted to the blue. We interpret this result in terms of a double-peak structure observed in the [O III] lines in the region that is coincident with the [Fe VII] emission. We also discard that the low velocity dispersion is due to the fact that the gas is along the galaxy disc. Indeed, it is a physically connected to the region that goes along the radio-jet, which is nearly perpendicular to the galaxy disc.

We also observe a negative radial trend for the velocity and the velocity dispersion of the broad component. As pointed out by Karouzos et al. (2016), the negative radial trend of the broad [O III] component indicates non-gravitational effects such as outflows, whose velocity decreases radially. Still, the prevalence of negative velocities in the broad component indicates that we preferentially see the approaching component of the outflow. However, at some positions, we clearly see both the approaching and receding components of the outflow.

It is also interesting to note that the bulk of the outflow is characterised by relative small values of velocity dispersion ($\sigma \sim 200$ km s^{-1}) with moderate shifts, of up to −200 km s^{-1} . Outflowing gas with the above characteristics is also emitting [Fe VII], with similar line shifts and velocity dispersion. More extreme [O III] outflowing gas ($\sigma > 250$ km s^{-1} and V< −200 km s^{-1}) has no counterpart in the coronal gas. This is probably due to S/N issues, as the [Fe VII] line is about an order of magnitude weaker relative to [O III].

We interpret the above results in terms of the launching point

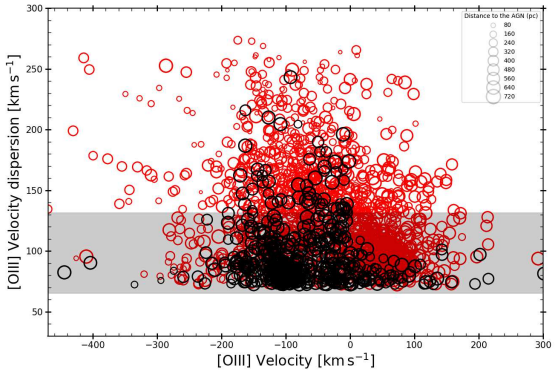

Figure 21. VVD diagram of the narrow (black) and broad (red) components of [O III] measured in individual spaxels of the ionisation cone of Circinus. The symbol size indicates the radial distance from the AGN (see the box at the upper right corner of the panel). The horizontal shaded area indicates the σ_* values measured from the CaT absorption lines (see Sect. 4.1).

of the outflow: the highest ionised portion of the outflow in Circinus is not launched at the AGN position but locally, likely inflated by the passage of the radio-jet. Another alternative is that it is produced by a stellar wind. However, the global star-formation rate in Circinus seems to be moderate (3 to 8 M⊙ yr^{-1}, For et al. 2012) to produce stellar outflows extending over scales of hundred of parsecs.

In summary, the data presented in this section point out to the presence of an ionised outflow in Circinus, with the NW side out of the galaxy plane and dominated by the approaching component. Part of the outflow is likely originated by a wind launched by the AGN. However, the highest-ionised portion of the outflow is most likely produced by a bubble of ionised gas inflated by the passage of the radio-jet.

5 DETERMINATION OF THE MASS OUTFLOW RATE

Determinations of the mass and outflow rate are traditionally carried out using the [O III] line. However, in the case of Circinus, it is difficult to separate the contribution of [O III] produced by the disc of the galaxy from that of the outflow. This difficulty is due to the fact that the galaxy disc appears in background relative the outflowing gas. Mingozzi et al. (2019) used a velocity criterion of [O III], where solely components with values smaller than -150 km s^{-1} and larger than 150 km s^{-1} (relative to the systemic velocity of the galaxy) would contribute to the outflow. However, Rodríguez-Ardila & Fonseca-Faria (2020) presented the velocity map of the [Fe VII]λ6087 gas and found that the outflow velocity determined from that line would have values -150 km s^{-1} < v < 150 km s^{-1} in most of the region where it is located. Assuming that [Fe VII]λ6087 entirely represents the outflowing gas, [O III] and [Fe VII] emissions are expected to agree in velocity on each spaxel if the only contribution is the outflow. Therefore, the [O III] emission attributed solely to the disc component by Mingozzi et al. (2019) should also contribute to the outflow. Thus, for the calculation of the outflow mass in Circinus, we assume that the contribution of [O III] in the region co-spatial with [Fe VII] is dominated by the outflow component.

5.1 Calculation of outflow in a model for a biconic structure

We first calculated the outflow rate and the mass of the outflow for the high ionisation region traced by the [Fe VII] line. To this purpose, a mask was initially generated in the region where the high ionisation gas is found allowing to calculate the integrated flux of the [O III] line in that region. For the results obtained here we use the calculations presented by Cano-Díaz et al. (2012) given by Equation 5.

$$M_{ion}^{out} = 5.3\times10^{7}\,\frac{L_{44}([OIII])}{n_e 10^{[O/H]}}(M\odot) \tag{5}$$

where $L_{44}([OIII])$ is the luminosity of the [O III] line which contributes to the outflow in units of 10^{44} erg s^{-1}, n_e is the gas density in units of 10^3 cm^{-3}, v_3 is the outflow speed in units of 10^3 km s^{-1} and $R_{\rm Kpc}$ is the radius, in kpc, of the biconical region which participates in the outflow. Thus, from the mask of the [Fe VII] region we found a [O III] flux for a blue and red components of 2.7×10^{-12} erg s^{-1} cm^{-2} Spaxel^{-1} and 2.4×10^{-12} erg s^{-1} cm^{-2} Spaxel^{-1}, respectively. The corresponding gas luminosity is 1.5×10^{6} L⊙ (i.e. 5.7×10^{39} erg s^{-1}) and 1.3×10^{6} L⊙ (i.e. 5.1×10^{39} erg s^{-1}). We thus find an outflow rate for the blue and red components of 0.12 M⊙ yr^{-1} and 0.10 M⊙ yr^{-1}. The mass of the gas involved in the outflow is 10^4 M⊙ and 9×10^3 M⊙, for the blue and red components, respectively.

5.2 Calculation of outflow rate using the $H\beta$ emission

We also estimated the mass and outflow rate using the flux of Hβ following a method presented by Santoro et al. (2018). The ionised gas mass can be estimated by the Equation 6.

$$M_{gas} = \frac{L(H_\beta)m_p}{n_e\alpha_{H\beta}^{eff}h\nu_{H_\beta}} \tag{6}$$

Where $L(H\beta)$ represents the luminosity of the Hβ line, m_p is the mass of the proton (1.673×10^{-27} kg), n_e is the gas electron density (~ 300 cm^{-3}), $\alpha_{H\beta}^{eff}$ is the effective recombination coefficient for Hβ (we use 3.03×10^{-14} cm^3 s^{-1}, for case B, (Osterbrock & Ferland 2006)), $h\nu_{H_\beta}$ is the frequency of the Hβ line (4861.3 Å) and h is Planck constant ($6,626\times10^{-34}$ J.s). The outflow rate was estimated using Equation 7. The calculations herewith are presented in detail by Rose et al. (2018).

$$\dot{M}_{gas} = \frac{L(H_\beta)m_p v_{out}}{n_e\alpha_{H\beta}^{eff}h\nu_{H_\beta}r} \tag{7}$$

In Equation 7 the term v_{out} represents the expansion velocity of the outflow. Here, we assume a value of ~ 750 km s^{-1}), derived from the channel maps of [O III]. The term r is the gas shell radius of the expanding outflow (200 parsec). We found a Hβ flux for the blue and red components of 2.9×10^{-13} erg s^{-1} cm^{-2} Spaxel^{-1} and 2.4×10^{-13} erg s^{-1} cm^{-2} Spaxel^{-1} respectively. In terms of luminosity, these values translate into 1.6×10^{5} L⊙ (i.e. 6.1×10^{38} ergs s^{-1}) and 1.4×10^{5} L⊙ (i.e. 5.1×10^{38} ergs s^{-1}). Thus, we find an outflow rate for the blue and red components of 0.05 M⊙ yr^{-1} and 0.04 M⊙ yr^{-1} and a mass of gas of 1.4×10^4 M⊙ and 1.2×10^4 M⊙, respectively.

6 MODELLING THE SPECTRAL LINE RATIOS

In the preceding sections, we have accumulated compelling observational evidence of the presence of a radio jet interacting with the ionisation cone ISM in Circinus. Although the jet has not been imaged at high-resolution, the detection of extended highly-ionised gas as well as the peculiar kinematics exhibited by [O III] λ5007 suggest the presence of localised jet-driven shocks across the region where the extended, high-ionisation emission is detected.

We investigate if shocks can indeed power much of the coronal line emission observed in the Circinus ionisation cone. Note that by no means we are discarding the influence of the radiation from the central source. Its effects, however are mostly restricted to the low-ionisation gas. For instance, we have seen in Fig. 8 the increase of the gas ionisation with increasing distance from the AGN. Moreover, the enhancement of the gas ionisation is preferentially observed in the directions where the jet has presumably crossed the ionisation cone. To study the main source of gas ionisation in Circinus, we selected 11 different regions located within the ionisation cone. Seven of them include areas where the highest ionisation gas, as probed by the [Fe VII] λ6087 line, is observed. We also include regions along the edges of the ionisation cone, as traced by [O III] as well as clumps with bright [Fe VII] and [Fe X] emission. Figure 22 shows the 11 selected regions marked with red boxes in addition to region R6a, which is centred at the nucleus of Circinus.

The observed lines and the ionisation potentials (IP) relative to their ions are given in Table 1. The IPs are ordered with decreasing energies to give a hint about the distribution of the physical parameters throughout the observed regions.

Fig. 22 shows, at a first glance, some interesting issues. Four regions, characterised by the highest ionisation lines, are revealed by [Fe X]. They are identified as R1a, R5b, R6a and R6b. [Fe VII]/Hβ is relatively strong in the R1a region, increasing towards the North-West (R1b, R2a, and R3). [Ar III]/Hβ , [O III]/Hβ , and [S III]/Hβ have similar intensity-ratio distributions covering all the regions named R1, R2, R3, R4, and R5 with smooth differences. This extended emission is divided in different regions according to the distribution of the [Fe VII]/Hβ, [O I]/Hβ, and [N II]/Hβ line ratios (see Fig. 8). In particular, the [N II]/Hβ map indicates a kind of "jet-driven" region in R3. This is because it is characterised by a relatively low line ratio. The same can be said for the [S III]/Hβ map, although with lower values. In the opposite position (South-East) the detached 'island' (R6) shows a concentric distribution with a high [Fe X]/Hβ and [O III]/Hβ core (R6a) decreasing towards the edge (R6b). [O II]/Hβ has a fragmented structure, most likely depending on the relatively low critical density for collisional deexcitation. A region of slightly enhanced low ionisation-level lines can be seen in the [O I]/Hβ , [S II]/Hβ , and [O II]/Hβ maps at the South-West. It is identified as R8 in Fig. 22. On the other hand, [O II]/Hβ disappears in the North-East where [S II]/Hβ and [O I]/Hβ are still relatively high (reported as R7). Regions R7 and R8 show the spectroscopic characteristics of the ISM.

Tables 1 to 12 list the average FWHM (column 2), the maximum FHWM averaged over all the spaxels in the region (column 3) and the maximum FWHM (column 4) measured for the different emission lines in each region defined by its coordinates (ΔX / ΔY). The scatter in FWHM for each region reveals that the observed values are the results of the contribution of many clouds with different physical conditions. Therefore, to reproduce the observations for the averaged line ratios in the different regions, we employed for the calculation of the spectra the code SUMA (Contini & Viegas 2001), which accounts for the coupled effect of shock and photoionisation by the central source. The code and the input parameters are briefly described in Sect. 6.1.

Figure 23 shows the location of the R1-R8 regions selected for our analysis in the traditional BPT diagrams [N II]/Hα vs [O III]/Hβ (upper panel) and [S II]/Hα vs [O III]/Hβ (bottom panel) proposed by Veilleux & Osterbrock (1987). In both plots, the line that separates the AGN domain from the star-formation and H II regions is taken from Veilleux & Osterbrock (1987). Note that only the average spectrum from region R2b is on the border line between AGN and star-forming region. All other observed ratios are in the AGN-dominated region.

Each one of the R1-R8 region spectra cover lines from different ionisation levels. Relatively high values of [Fe VII]/Hβ and [O I]/Hβ can be hardly fitted by a single model. We have chosen to reproduce the spectrum in each region by the contribution of two representative models. One, shock dominated (SD), is calculated considering that the flux from the active centre (AC) is zero, i.e. it does not reach the emitting gas. The other model, radiation dominated (RD), assumes that the radiation from the AC dominates although shocks are also at work. A perfect fit to the spectra of the different regions is not expected because too many different physical conditions coexist throughout the observed regions. RD models are radiation bounded, therefore, they are adapted to reproduce all the line ratios in each spectrum except lines from the high ionisation levels. In fact, relatively high temperatures of the emitting gas adapted to high [Fe VII] and [Fe X] line emission fluxes appear in the region near the shock front downstream even for the RD models, depending on the shock velocity. The temperature downstream decreases throughout the gaseous clouds following the cooling rate which yields gas recombination. In a large region of gas the temperature is maintained $\geq 10^4$ K by radiation from the AC and by secondary radiation. Therefore lines from medium and low ionisation levels (e.g. Hβ) are strong and the calculated [Fe VII]/Hβ and [Fe X]/Hβ ratios are low compared with the observed ones. On the other hand, relatively high [Fe X]/Hβ and [Fe VII]/Hβ , [Ar X]/Hβ and [Ar V]/Hβ are better reproduced by matter-bounded SD models. As an example, we show in Figs. 24 and 25 the profiles for electron temperature, electron density and fractional abundances of the most significant ions throughout a RD and a SD cloud (mRD1a and mSD1b in Table 1, respectively) ejected outwards from the AC.

In Fig. 24 the nebula is divided into two halves. The shock front is on the left side of the left panel, while the edge reached by the photoionising flux from the AC is on the right of the right panel, opposite to the shock front. In the right panel of Fig. 24 the X-axis scale is logarithmic and reverse in order to show with the same precision the physical conditions at the two edges of the cloud. The shock dominated and the radiation dominated sides of the emitting nebula are bridged by secondary radiation, produced by the slabs of gas heated by the shock, leading to a large zone of gas at T$\sim 10^4$K. In the SD dominated clouds (Fig. 25), the internal edge opposite to the shock front shows the cool gas recombined region. The downstream region throughout the cloud is interrupted before recombination of high-level ions such as Fe^{6+} and Fe^{9+} and also to avoid a strong Hβ line intensity, which could reduce the [Fe VII]/Hβ and the other high-ionisation line ratios. Moreover, a pure shock model radiation-bounded would lead to relatively high [O II]/Hβ line ratios. In the top panel of Fig. 25 we have marked by a dotted vertical line the distance from the shock front at which the calculations stop for model mSD1b. The choice of the shock velocity in SD models is constrained by the observed [Fe VII]/[Fe X] and [Fe VII]/Hβ line ratios.

Some elements (e.g. S and N) can be depleted from the

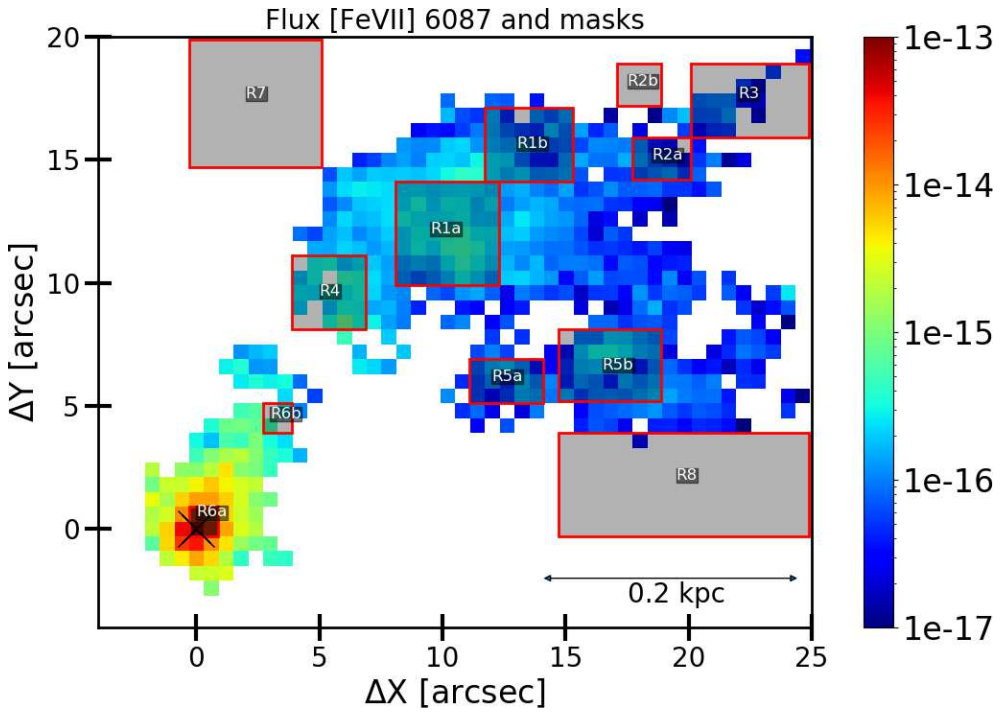

Figure 22. In colour scale we show the [Fe VII] λ6087 emission. Twelve regions, bounded in red, were selected as representative of the ionisation cone. The colour bar is in erg cm^{-2} s^{-1} spaxel^{-1}.

Table 1. Ionisation potentials of different level ions.

line	[Ar x]	[Fe x]	[Fe VII]	[Ar v]	[O III]	HeII	[Ar III]	[O II]	[S III]	[N II]	HeI	[S II]	[O I]
λ(Å)	5533	6375	6087	7006	5007	5412	7136	7320	9069	6583	6678	6716	6300
IP (eV)	422.6	233.6	99.0	59.6	35.5	54.4	27.6	13.6	23.3	14.5	24.6	10.4	0

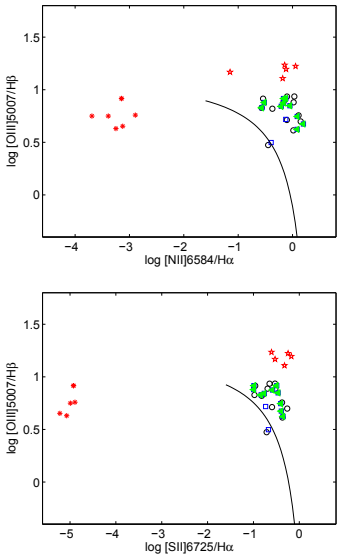

Figure 23. BPT diagrams [O III]/Hβ vs [N II]/Hα (upper panel) and [O III]/Hβ vs [S II]/Hα (bottom panel) for line ratios presented in Table 2. Black open circles are the observed data; blue open squares are the results of RD models; green triangles represent averaged results; red asterisks represent matter-bounded SD models while red stars show the shock dominated region (radiation-bounded models).

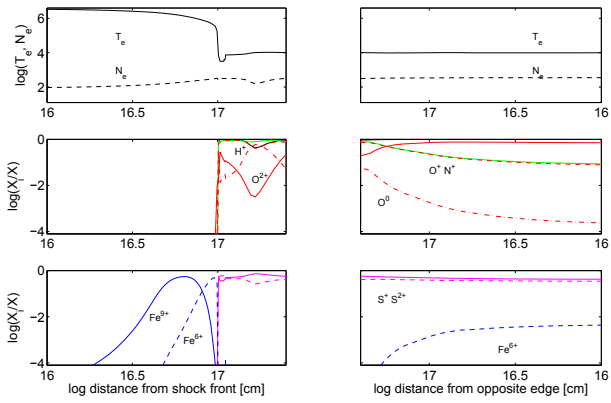

Figure 24. The profiles of T_e, n_e, and of the fractional abundance of the most significant ions throughout the clouds in region R1a calculated by a RD model.

gaseous phase because they are trapped into dust grains and into molecules. The grains are sputtered throughout the shock front and downstream depending on the shock velocity. Therefore, the abundances of the heavy elements relative to the solar value can change from model to model. For the other elements (He, C, O, Ne, Mg,

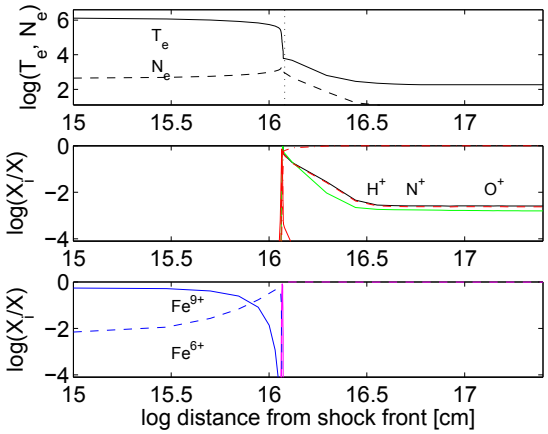

Figure 25. The profiles of T_e, n_e, and of the fractional abundance of the most significant ions throughout the clouds in region R1b calculated by a SD model.

Si, Ar, Cl, and Fe) solar abundances relative to H (Asplund et al. 2009) were adopted.

6.1 Calculation details

The main input parameters adopted to model the 12 integrated emission line regions marked in Fig. 22 are those that lead to the best fit of calculated to observed line ratios and continuum emission fluxes. SUMA accounts for photoionisation and heating by primary and secondary radiation and for collisional processes due to shocks.

The input parameters such as the shock velocity V_s , the atomic preshock density n_0, and the preshock magnetic field B_0 (for all models $B_0 = 10^{-4}$ Gauss is adopted) define the hydrodynamical field. They are combined in the compression equation, which is resolved throughout each slab of gas in order to obtain the density profile across the emitting clouds. The AGN photoionising continuum radiation is represented by a power-law radiation flux F in number of photons cm^{-2} s^{-1} eV^{-1} at the Lyman limit and spectral indices α_{UV} = -1.5 and α_X = -0.7. The primary radiation source does not depend on the host galaxy physical conditions but it affects the surrounding gas. This region is not considered as a unique cloud, but as a sequence of plane-parallel slabs (up to 300) with different geometrical thickness calculated automatically following the temperature gradient. The secondary diffuse radiation is emitted from the slabs of gas heated by both the radiation flux reaching the gas and the shock. Primary and secondary radiation are calculated by radiation transfer. The calculations initiate at the shock front where the gas is compressed and adiabatically thermalised, reaching a maximum temperature in the immediate post-shock region $T \sim 1.5\times10^5$ (V_s /100 km s^{-1})^2. T decreases downstream, leading to gas recombination. The cooling rate is calculated in each slab. The line and continuum emitting regions throughout the galaxy cover an ensemble of fragmented clouds. The geometrical thickness D of the clouds is an input parameter that is calculated consistently with the physical conditions and element abundances of the emitting gas.

The fractional abundances of the ions are calculated resolving the ionisation equations for each element (H, He, C, N, O, Ne, Mg, Si, S, Ar, Cl, Fe) for each ionisation level. Then, the calculated line ratios, integrated throughout the cloud geometrical width, are compared with the observed ones. The calculation process is repeated, changing the input parameters until the observed data are reproduced by model results, at maximum within 10-20 percent for the strongest line ratios and within 50 percent for the weakest ones.

6.2 Modelling results

In Table 2 the average observed line ratios (marked with the sufix "obs") are presented. They are compared with RD and SD model results in the following two rows. In the next row the weighted sum of the calculated line ratios are reported. The models were constrained by the [O III]/Hβ , [Fe VII]/Hβ , [N II]/Hβ , [S II]/Hβ , and [O II]/Hβ line ratios. The models are described in Table 3. The last column of that table shows the Hβ fluxes calculated at the nebula (Hβ_c). It allows us to calculate the line flux intensities for each line using the line ratios of Table 2 and eventually add up the RD and SD model contributions in each region by the relative weights.

Dividing the total flux calculated for each line by the Hβ_c weighted sum, we obtain the results for the total line ratios. They can be compared to the observed data in Table 2. The total Hβ line flux calculated at the nebula and the relative weights w adopted to add up the RD and SD model results are given in the two bottom lines of Table 4, respectively. The R2b and R4 spectra are reproduced by only the RD model.

As mentioned above, the SD models that appear in Table 2 are matter-bounded in order to obtain the [Fe VII]/Hβ and [Fe X]/Hβ line ratios suitable to the averaged models. In the bottom 5 lines of Table 2 we report the line ratios calculated by the by the corresponding radiation-bounded SD models that we obtained using a cloud geometrical thickness D >0.1 pc for all of them. Model m104 was used to fit the spectra of R1a, R3, R5a, R5b and R6a while model m101 better reproduces R1b and R6b. Model m100 fits R2a, whereas models m107 and m108 are suitable to the R7 and R8 regions. Radiation-bounded SD models are calculated in order to show the shock dominated region in BPT diagrams for relatively high shock velocities $V_s \geq 100$ km s^{-1} . Lower velocities are more adapted to star-formation and HII regions.

Our results show that not always low O/H, N/H and S/H translate into low [O III]/Hβ , [N II]/Hβ , and [S II]/Hβ ratios in the BPT diagrams. The geometrical thickness of the emitting cloud plays a key role in the modelling.

The results obtained by modelling the observation data in the different regions are commented below.

(i) Table 2 indicates that for all the observed regions, [Fe VII]/[Fe X] > 1. Model results show that this constraint is achieved by $V_s \leq 550$ km s^{-1} . The good fit to the observed [Fe VII]/Hβ confirms our hypothesis that SD models are radiation bounded. [Fe X] lines are weaker and indeed seldom observed.

(ii) Different relative weights are adopted in different regions (See Table 4 to sum the SD and RD cloud contributions). In regions R1a and R6a, the [Ar X] λ5533/Hβ is higher by a factor of > 100 than in the other regions. At the relatively high velocities observed from the [Ar X] line profile, this line can be blended with [Cl III] λ5539. [Cl III]/Hβ results 0.02 and 0.025 in the R1a and R6a regions, respectively.

(iii) Regarding the preshock density, we have found that RD models are constrained by the [O II] λ7320/Hβ line ratios, which are ≤0.1 in all the observed regions. This threshold is achieved by clouds of relatively low n_0, ~20-60 cm^{-3} . In Table 4, T_e and n_e in each region are calculated from the average observed data reported in Table 2. It can be seen that n_e are roughly proportional to n_0 for RD model results, recalling that in the downstream region through-

out the clouds the gas is compressed by factors of 5-10, depending on the shock velocity and the magnetic field. SD models are less constrained by the choice of n_0 because in matter-bounded models the [O II] λ7320/Hβ line ratio is always < 1. The preshock densities adopted in this work agree with those obtained by fitting the Circinus galaxy observed spectra by Contini et al. (1998).

(iv) We have reproduced the O, Ar and Fe line ratios to Hβ by solar abundances relative to H (6.6×10^{-4}, 3.27×10^{-6} and 3.2×10^{-5}, respectively). The N/H solar relative abundance (10^{-4}) was altered by factors of 0.4-1.8 to improve the fit of the corresponding line ratios. The S/H relative abundances were found lower than solar (2×10^{-5}) in all the observed regions, due to the presence of dust.

(v) The Hβ_c flux calculated by SD models results lower by factors between < 10 and > 100 than for RD models because SD models are matter bounded. High fragmentation of the clouds may be explained by turbulence created by shocks at the shock-fronts.

(vi) The photoionisation flux from the AC is relatively low throughout the observed regions, similar to F found for LINERS. In particular, it declines in the external regions R7 and R8.

6.3 Discussion

High energy emission lines with an X-ray emission counterpart is indicative of photoionisation by a central source as the dominant ionisation process (Rodríguez-Ardila et al. 2011). In the work of Ferguson et al. (1997), the minimum and maximum distances suitable to find high ionisation lines from a cloud photoionised by the central source are presented. For example, for the [Fe VII] λ6087 line, the models predict an upper limit of 110 pc from the AGN. Here, we found that this line in Circinus extends to distances of up to 700 pc, ruling out the possibility of being produced by the central source alone. Moreover, the extended coronal emission is coincident with the central portion of the ionisation cone. Kinematics evidence show that this HIG is out of the galaxy plane. The predicted size of the emission regions of [Fe X] and [Ar X] are even smaller than that of [Fe VII] under a central source photoionisation scenario: They are limited to 20 pc and 1 pc, respectively. However, we clearly detect both (see Fig.7) at distances larger than 140 pc in the nuclear region, and up to 370 pc in the extended outflow. This result further supports our hypothesis that an additional mechanism must be at work to power that coronal emission.

The photoionisaton code SUMA (Contini & Viegas 2001), which couples the effect of photoionisation by the central source and shocks, show that the [Fe VII] λ6087 line can be produced away from the AC when the shock velocities are > 200 km s^{-1}. We measure from MUSE values much higher than that, as can be seen in Figure 17. Note though, that values of shock velocities and gas velocities do not necessarily need to match. Figure 9 shows evidence of a higher electron temperature at the edges of the [Fe VII] clouds and that the temperature of the red component appears to be lower than that of the blue component. This is in line with the concept of a possible precursor gas. In this case we are assuming that the gas did not have time to cool down and we see the effect of the precursor. Following the hypothesis that a precursor is photoionising the gas of the red component in Figure 9, the shocked gas in the region of the blue component has not yet reached the region of the red component. It may be suggestive of a jet that has already passed and cooled. Apparently, the same effect as that we are seeing in the blue component will be found for the red component in a few thousand years.

7 CONCLUDING REMARKS

Detailed analysis of MUSE data allowed us to study, for the first time in the literature, the high-ionised outflow detected by means of the [Fe VII] λ6087 line in the Circinus Galaxy. The emission fills the central portion of the prominent NW ionisation cone and is clearly aligned to the radio jet. The coronal gas extends at least up to 700 pc from the nucleus although we do not discard that it extends further out. Moreover, we report on the first confirmed detection of extended [Fe X] λ6374 gas in Circinus. That emission is produced by an extended cloud of several tens of parsecs size, clearly resolved with MUSE and visible up to ~350 pc from the nucleus. The region where the extended emission is observed coincides in position with the brightest portion of the extended [Fe VII] gas.

We examined the behaviour of the different emission line flux distributions relative to Hβ. The results show that most of the high-ionisation lines are enhanced in the extended [Fe VII] region. In contrast, low-ionisation lines are weak relative to Hβ in the region dominated by the extended coronal emission, becoming stronger outside the region filled with the high-ionisation gas. This result suggests an additional mechanism at work favouring the coronal line production.

Kinematic evidence as well as the examination of the physical conditions of the high-ionised outflow indicates that it is out of the galaxy plane, following non-circular motions. All evidence suggests that it is likely produced by a radio jet that passed through the region, inflating the gas and producing expanding bubbles, seen in the form of approaching and receding gas shells. These structures display velocities of a few hundred km s^{-1}, spatially coincident with prominent hard X-ray emission detected by Chandra. Density and temperature sensitive line ratios show that the extended high-ionisation gas is characterised by temperatures of up to 25000 K and electron density $n_e > 10^4$ cm^{-3}. We do not discard some contribution from stellar winds, given that molecular outflows have been detected with ALMA in projection with the ionisation cone.

The above scenario is further supported by means of ionisation models that couple the effects of central source photoionisation plus shocks. The good fit to the observed [Fe VII]/Hβ confirms our hypothesis that shock-dominated clouds must be present in the ionisation cone of Circinus. These clouds are responsible for the bulk of the extended coronal emission. Shock velocities with $V_s > 200$ km s^{-1} are required for the production of such lines, in agreement with the observed gas kinematics.

Overall, our analysis find compelling evidence that the innermost portion of the ionisation cone in Circinus is jet-driven. It also demonstrates the role of low-power radio jets in a low-luminosity AGN, being able to produce outflow rates of order of 0.4 M$\odot$ yr^{-1}, similar to the ones observed in sources of higher luminosity. Detailed analysis of similar sources are needed in order to quantify the relevance of the kinetic channel in the feedback of active galactic nuclei.

ACKNOWLEDGEMENTS

We are grateful to the anonymous Referee for useful comments and suggestions to improve this manuscript. ARA acknowledges Conselho Nacional de Desenvolvimento Científico e Tecnológico (CNPq) for partial support to this work through grant 312036/2019-1.

Table 2. Comparison of the calculated line ratios to Hβ with the observed average in the different regions.

Region	[O III] 5007	[Ar x] 5533	[Fe VII] 6087	[O I] 6300	[S III] 6312	[Fe x] 6375	Hα 6563	[N II] 6583	[S II] 6717	[Ar v] 7006	[Ar III] 7136	[O II] 7320	[S III] 9069
R1a (obs)	10.31	0.02	0.12	0.23	0.04	0.02	3.10	2.13	0.63	0.07	0.27	0.06	0.45
mRD1a	10.0	3E-4	0.022	0.1	0.03	0.005	2.92	2.	0.76	0.007	0.3	0.09	0.6
mSD1a	11.	0.03	13.3	0.0	0.002	0.9	4.2	0.003	0.0	0.9	0.02	0.03	0.0
mR1a	10.	5.E-4	0.11	0.1	0.03	0.01	2.93	2.	0.75	0.013	0.3	0.09	0.59
R1b (obs)	8.8	-	0.22	0.12	0.03	-	3.1	1.32	0.47	0.07	0.2	0.06	0.35
mRD1b	9.3	3.E-4	0.024	0.1	0.02	0.006	2.9	1.8	0.5	0.006	0.35	0.1	0.4
mSD1b	7.5	6.4E-4	15.6	0.0	6.E-4	0.014	4.9	0.001	0.0	1.2	0.011	0.01	0.002
mR1b	9.27	3.E-4	0.24	0.1	0.02	0.006	2.93	1.8	0.5	0.02	0.34	0.1	0.4
R2a (obs)	8.97	-	0.22	0.07	-	-	3.23	0.87	0.34	0.09	0.21	-	0.37
mRD2a	9.	3E-5	0.027	0.05	0.028	6E-5	2.92	0.80	0.43	0.004	0.37	0.1	0.6
mSD2a	7.65	0.09	12.3	1.E-5	0.002	2.	3.9	0.005	5E-5	0.07	0.012	0.02	0.02
mR2a	8.97	0.0014	0.22	0.05	0.027	0.03	2.94	0.79	0.42	0.005	0.36	0.1	0.06
R2b (obs)	3.97	-	-	0.17	-	-	3.09	1.1	0.60	-	0.19	0.37	-
mRD2b	4.2	1.3E-5	0.017	0.2	0.007	3.E-6	2.97	1.2	0.63	0.003	0.18	0.27	0.46
R3 (obs)	10.96	-	0.22	0.13	-	-	3.38	0.97	0.37	0.09	021	0.14	0.32
mRD3	10.1	6.5E-5	0.05	0.01	0.04	1.E-4	2.97	0.9	0.3	0.01	0.38	0.13	0.9
mSD3	11.	0.03	13.3	0.0	0.02	0.9	4.2	0.003	0.0	0.94	0.013	0.034	0.0
mR3	10.1	4.E-4	0.22	0.01	0.04	0.01	2.98	0.9	0.3	0.02	0.37	0.128	0.89
R4 (obs)	6.88	-	0.03	0.2	0.02	-	3.11	2.45	0.79	0.02	0.114	0.05	0.22
mRD4	6.97	4E-5	0.03	0.05	0.03	0.0	2.93	2.2	0.54	0.003	0.3	0.09	0.9
R5a (obs)	10.12	-	0.08	0.32	0.04	-	3.10	3.25	0.93	0.04	0.25	0.11	0.50
mRD5a	9.4	1E-4	0.02	0.24	0.03	0.001	2.9	2.6	1.0	0.005	0.3	0.11	0.6
mSD5a	11.	0.03	13.3	0.0	0.002	0.9	4.2	0.003	0.0	0.94	0.02	0.034	0.0
mR5a	9.4	2.4E-4	0.082	0.24	0.03	0.005	2.9	2.6	1.	0.009	0.3	0.11	0.6
R5b (obs)	11.49	-	0.09	0.20	0.04	0.01	3.12	2.47	0.7	0.04	0.3	0.06	0.58
mRD5b	11.0	3E-6	0.044	0.01	0.04	0.006	2.93	2.	0.3	0.01	0.33	0.06	0.9
mSD5b	11.0	0.03	13.3	0.0	0.002	0.9	4.2	0.003	0.0	0.94	0.02	0.034	0.0
mR5b	11.	1E-4	0.09	0.01	0.04	0.01	2.93	2.	0.3	0.013	0.33	0.06	0.89
R6a (obs)	11.5	0.04	0.15	0.62	0.03	0.13	3.12	3.37	0.92	0.03	0.25	0.11	0.44
mRD6a	11.0	3E-4	0.02	0.4	0.035	0.005	2.92	2.2	0.94	0.007	0.35	0.1	0.7
mSD6a	11.0	0.03	13.3	0.0	0.002	0.9	4.2	0.003	0.0	0.94	0.02	0.034	0.0
mR6a	11.	6.E-4	0.16	0.4	0.034	0.014	2.94	2.2	0.93	0.02	0.35	0.1	0.69
R6b (obs)	7.6	-	0.06	0.46	0.02	0.02	3.11	4.02	1.31	-	0.18	0.09	0.21
mRD6b	7.42	1.2E-4	0.02	0.34	0.02	0.002	2.94	3.6	1.16	0.003	0.28	0.12	0.5
mSD6b	7.5	6.E-4	15.6	0.0	6.E-4	0.014	4.9	0.002	0.0	1.26	0.011	0.015	0.002
mR6b	7.42	1.2E-4	0.051	0.34	0.02	0.002	2.94	3.6	1.16	0.006	0.28	0.12	0.5
R7 (obs)	5.48	-	-	0.43	-	-	3.8	3.93	1.63	-	0.16	0.09	0.25
mRD7	5.6	3E-4	0.023	0.4	0.02	0.005	2.95	3.6	1.3	0.003	0.25	0.09	0.4
mSD7	5.7	0.14	11.8	0.0	9E-4	3.0	3.9	2.2E-3	3.3E-5	0.67	0.09	0.07	0.003
mR7	5.6	8.E-4	0.06	0.4	0.02	0.02	2.96	3.6	1.3	0.005	0.25	0.09	0.4
R8 (obs)	6.66	-	0.09	0.59	-	-	3.74	5.28	2.04	-	0.26	0.19	0.40
mRD8	6.3	1.3E-4	0.023	0.64	0.02	0.002	2.96	4.7	1.2	0.004	0.23	0.18	0.4
mSD8	6.	0.04	12.8	0.0	6E-4	1.2	4.	0.003	2.4E-5	0.7	0.09	0.01	0.005
mR8	6.3	2.E-4	0.09	0.64	0.02	0.008	3.	4.7	1.2	0.007	0.23	0.18	0.40
m100	17.1	7.e-3	1.07	0.42	0.1	0.17	5.0	3.3	2.38	0.08	0.15	4.3	0.3
m101	22.9	4e-5	0.91	0.44	0.11	8e-4	5.85	4.2	1.45	0.12	0.2	7.25	0.3
m104	19.6	3.e-3	1.12	0.44	0.1	0.079	5.5	0.39	1.63	0.1	0.2	6.	0.34
m107	20.9	0.014	1.13	0.27	0.13	0.29	4.86	3.7	3.26	0.09	0.19	3.59	0.45
m108	22.3	4.-3	1.24	0.34	0.11	0.12	5.27	6.0	3.0	0.1	0.2	3.89	0.4

DATA AVAILABILITY

The data underlying this article are available in the European Southern Observatory archive. The data can be obtained in raw quality through the MUSE raw data query form (http://archive.eso.org/wdb/wdb/eso/muse/form). Science quality data can be obtained from the Spectral data products query form http://archive.eso.org/wdb/wdb/adp/phase3spectral/form?collectionname=MUSE.

REFERENCES

Asplund M., Grevesse N., Sauval A. J., Scott P., 2009, ARA&A, 47, 481.
Bertola F., Bettoni D., Danziger J., Sadler E., Sparke L., de Zeeuw T., 1991, ApJ, 373, 369
Bruzual G., Charlot S., 2003, MNRAS, 344, 1000
Cano-Díaz M., Maiolino R., Marconi A., Netzer H., Shemmer O., Cresci G., 2012, A&A, 537, L8
Cappellari M., Emsellem E., 2004, PASP, 116, 138
Cardelli J. A., Clayton G. C., Mathis J. S., 1989, ApJ, 345, 245
Cid Fernandes R., Mateus A., Sodré L., Stasińska G., Gomes J. M., 2005,

Table 3. Input parameters of the models for each of the regions analysed.

	V_s km s^{-1}	n_0 cm^{-3}	D pc	F units^2	N/H 10^{-4}	S/H 10^{-4}	Hβ_c ^{1} erg cm^{-2} s^{-1}
mRD1a	500	20	0.14	2.	1.	0.12	3.3E-3
mSD1a	270	180	0.0015	-	1.	0.1	2.6E-5
mRD1b	500	20	0.13	1.7	1.	0.08	3.3E-3
mSD1b	280	200	0.0005	-	1.	0.1	1.9E-5
mRD2a	200	40	0.05	1.2	0.4	0.1	1.8E-3
mSD2a	300	100	0.004	-	1.	0.12	1.8E-5
mRD2b	180	60	0.03	1.2	0.4	0.06	2.7E-3
mRD3	200	45	0.023	1.3	0.8	0.15	1.0E-3
mSD3	270	180	0.0015	-	1.	0.1	2.6E-5
mRD4	200	40	0.043	1.0	1.0	0.13	1.1E-3
mRD5a	260	41	0.067	2.7	1.4	0.13	4.4E-3
mSD5a	270	180	0.0015	-	1.	0.1	2.6E-5
mRD5b	300	30	0.05	1.5	1.8	0.16	1.5E-3
mSD5b	270	180	0.0015	-	1.	0.1	2.6E-5
mRD6a	550	20	0.17	2.7	1.	0.13	4.8E-3
mSD6a	270	180	0.0015	-	1.	0.1	2.6E-5
mRD6b	280	38	0.067	2.	1.	0.12	3.8E-3
mSD6b	280	200	0.0005	-	1.	0.1	1.9E-5
mRD7	350	20	0.17	0.86	1.	0.13	2.E-3
mSD7	350	20	0.03	-	1.	0.13	3.6E-6
mRD8	250	20	0.26	0.7	1.3	0.1	1.4E-3
mSD8	250	20	0.04	-	1.3	0.1	2.3E-6

[1] Hβ calculated at the nebula; [2] in 10^9 photon cm^{-2} s^{-1} eV^{-1} at the Lyman limit

MNRAS, 358, 363
Contini M., Prieto M. A., Viegas S. M., 1998, ApJ, 505, 621.
Contini M., Viegas S. M., 2001, ApJS, 132, 211
Contini M., Prieto, M. A., Viegas S. M., 1997, ApJ, 483, 887
Curran S. J., Johansson L. E. B., Rydbeck G., Booth R. S., 1998, A&A, 338, 863
Dasyra K. M., Bostrom A. C., Combes F., Vlahakis N., 2015, ApJ, 815, 34
Dasyra K. M., Combes F., Oosterloo T., Oonk J. B. R., Morganti R., Salomé P., Vlahakis N., 2016, A&A, 595, L7
Dopita M. A., Seitenzahl I. R., Sutherland R. S., Vogt F. P. A., Winkler P. F., Blair W. P., 2016, ApJ, 826, 150
Elmouttie M., et al., 1998, MNRAS, 297, 49
Elmouttie M., Haynes R. F., Jones K. L., Sadler E. M., Ehle M., 1998, MNRAS, 297, 1202
Esquej P., et al., 2014, ApJ, 780, 86
Ferguson J. W., Korista K. T., Ferland G. J., 1997, ApJS, 110, 287
Ferrarese L., Merritt D., 2000, ApJ, 539, L9
For B.-Q., Koribalski B. S., Jarrett T. H., 2012, MNRAS, 425, 1934
Frank J., King A., Raine D. J., 2002, in Accretion Power in Astrophysics, by Juhan Frank and Andrew King and Derek Raine, Cambridge University Press
Freeman K. C., Karlsson B., Lynga G., Burrell J. F., van Woerden H., Goss W. M., Mebold U., 1977, A&A, 55, 445
García-Bernete, I., Alonso-Herrero, A., García-Burillo, S., et al. 2020, A&A, accepted. arXiv:2009.12385
Gebhardt K., et al., 2000, ApJ, 539, L13
Greenhill L. J., et al., 2003, ApJ, 590, 162
Karouzos, Marios; Woo, Jong-Hak; Bae, Hyun-Jin., 2016, ApJ, 819, 148
Kormendy J., Richstone D., 1995, ARA&A, 33, 581
Kormendy J., Ho L. C., 2013, ARA&A, 51, 511
Maiolino R., et al., 2017, Nature, 544, 202
Marconi A., Moorwood A. F. M., Origlia L., Oliva E., 1994, Msngr, 78, 20
May D., Rodríguez-Ardila A., Prieto M. A., Fernández-Ontiveros J. A., Diaz Y., Mazzalay X., 2018, MNRAS, 481, L105
Meyer M. J., et al., 2004, MNRAS, 350, 1195
Mingozzi M., et al., 2019, A&A, 622, A146
Morganti R., Oosterloo T., Tsvetanov Z., 1998, AJ, 115, 915
Morganti R., Oosterloo T. A., Oonk J. B. R., Frieswijk W., Tadhunter C. N., 2015, ASP Conference Series Vol. 499. San Francisco: Astronomical Society of the Pacific, p.125
Müller Sánchez F., Davies R. I., Eisenhauer F., Tacconi L. J., Genzel R., Sternberg A., 2006, A&A, 454, 481
Oliva E., Marconi A., Moorwood A. F. M., 1999, A&A, 342, 87
Oosterloo T. A., Morganti R., Tzioumis A., Reynolds J., King E., McCulloch P., Tsvetanov Z., 2000, AJ, 119, 2085
Oosterloo T., et al., 2017, A&A, 608, A38
Osterbrock D. E., Ferland G. J., 2006, agna.book
Perna M., et al., 2015, A&A, 574, A82
Proxauf B., Öttl S., Kimeswenger S., 2014, A&A, 561, A10
Rodríguez-Ardila A., Viegas S. M., Pastoriza M. G., Prato L., 2002, ApJ, 579, 214
Rodríguez-Ardila A., Prieto M. A., Viegas S., Gruenwald R., 2006, ApJ, 653, 1098
Rodríguez-Ardila A., Prieto M. A., Portilla J. G., Tejeiro J. M., 2011, ApJ, 743, 100
Rodriguez-Ardila A., Fonseca-Faria M. A., 2020, ApJ, 895, 9L
Rose M., Tadhunter C., Ramos Almeida C., Rodríguez Zaurín J., Santoro F., Spence R., 2018, MNRAS, 474, 128
Ruiz M., Efstathiou A., Alexander D. M., Hough J., 2001, MNRAS, 325, 995
Santoro F., Rose M., Morganti R., Tadhunter C., Oosterloo T. A., Holt J., 2018, A&A, 617, A139
Schlafly E. F., Finkbeiner D. P., 2011, ApJ, 737, 103
Socas-Navarro H., 2015, A&A, 577, A25
Solórzano-Iñarrea C., Tadhunter C. N., 2003, MNRAS, 340, 705
Storchi-Bergmann T., Winge C., Ward M. J., Wilson A. S., 1999, MNRAS, 304, 35
Valentini M., Murante G., Borgani S., Granato G. L., Monaco P., Brighenti F., Tornatore L., et al., 2020, MNRAS, 491, 2779
Vazdekis A., Koleva M., Ricciardelli E., Röck B., Falcón-Barroso J., 2016, MNRAS, 463, 3409
Veilleux, Sylvain; Osterbrock, Donald E., 1987, ApJS, 63, 295
Veilleux S., Bland-Hawthorn J., 1997, ApJ, 479, L105
Wada K., Yonekura K., Nagao T., 2018, ApJ, 867, 49
Wilson A. S., Colbert E. J. M., 1995, ApJ, 438, 62
Woo, Jong-Hak; Bae, Hyun-Jin; Son, Donghoon; Karouzos, Marios., 2016, ApJ, 817, 108
Zakamska N. L., et al., 2016, MNRAS, 459, 3144
Zschaechner L. K., Walter F., Bolatto A., Farina E. P., Kruijssen J. M. D., Leroy A., Meier D. S., et al., 2016, ApJ, 832, 142

Table 4. Medium values of T_e and n_e, total Hβ_c and weights w calculated for the different regions modelled with SUMA.

	R1a	R1b	R2a	R2b	R3	R4	R5a	R5b	R6a	R6b	R7	R8
T_e (K) [1]	118884	10750	-	-	-	12692	11800	11065	10500	-	-	-
n_e (cm^{-3}) [2]	190	136	179	100	406	100	234	242	516	100	220	126
Hβ_{tot} [3]	3.33E-3	3.35E-3	1.83E-3	2.7E-3	1.13E-3	1.1E-3	4.4E-3	1.5E-3	4.85E-3	4.82E-3	2.E-3	1.4E-3
w	1	2.5	1.6	-	0.5	-	0.8	0.2	2	1	0.2	3.2

[1] T_e is obtained from [S III]λ9069/[S III]λ6312 [2] n_e is obtained from [S II]λ6716/[S II]λ6731; [3] in erg cm^{-2} s^{-1}

Table 1. FWHM measured in region R1a (ΔX/ΔY: 8"-12"/10"-14").

	FWHM[1,2]	max FWHM[1,2]	max FWHM[2]
[O III]λ5007	227.09	283.11	487.05
HeIIλ5412	201.78	205.36	607.22
[Ar X]λ5533	284.48	284.48	559.74
[Fe VII]λ6087	196.50	237.36	541.28
[O I]λ6300	185.51	239.16	522.33
[S III]λ6312	176.84	185.48	405.93
[O I]λ6364	204.99	204.99	517.25
[Fe X]λ6375	272.87	272.87	530.82
Hα λ6563	201.95	274.45	502.65
[N II]λ6583	175.23	229.31	466.03
HeIλ6678	250.34	263.44	494.12
[S II]λ6716	196.58	268.94	419.48
[Ar V]λ7006	173.00	202.94	432.77
[Ar III]λ7136	181.78	248.67	400.67
[O II]λ7320	216.15	251.08	647.57
[S III]λ9069	160.61	182.38	354.02

[1] average. [2] in km s^{-1}.

Table 2. FWHM measured in region R1b ΔX/ΔY: 12"-15"/14"-17".

	FWHM[1,2]	max FWHM[1,2]	max FWHM[2]
[O III]λ5007	238.07	298.36	654.85
HeIIλ5412	160.34	160.34	170.82
[Ar X]λ5533	208.82	208.82	425.95
[Fe VII]λ6087	208.44	237.79	429.15
[O I]λ6300	161.98	165.97	380.53
[S III]λ6312	143.07	143.07	170.48
[O I]λ6364	-	-	-
[Fe X]λ6375	235.34	235.34	530.82
Hα λ6563	206.53	275.76	502.65
[N II]λ6583	184.74	207.37	434.19
HeIλ6678	164.22	164.22	212.97
[S II]λ6716	203.46	273.07	491.36
[Ar V]λ7006	175.96	185.29	383.71
[Ar III]λ7136	177.54	200.93	462.73
[O II]λ7320	104.33	104.33	116.20
[S III]λ9069	216.16	216.16	298.11

[1] average. [2] in km s^{-1}.

Table 3. FWHM measured in region R2a ΔX/ΔY: 18"-20"/14"-16".

	FWHM[1,2]	max FWHM[1,2]	max FWHM[2]
[O III]λ5007	211.04	247.87	542.23
HeIIλ5412	-	-	-
[Ar X]λ5533	210.92	210.92	317.83
[Fe VII]λ6087	164.46	164.46	232.47
[O I]λ6300	124.02	124.02	124.02
[S III]λ6312	-	-	-
[O I]λ6364	-	-	-
[Fe X]λ6375	199.80	199.80	272.80
Hα λ6563	197.09	257.99	502.65
[N II]λ6583	193.77	203.19	299.39
HeIλ6678	-	-	-
[S II]λ6716	179.84	199.06	309.16
[Ar V]λ7006	159.28	159.28	221.86
[Ar III]λ7136	172.76	175.44	330.17
[O II]λ7320	-	-	-
[S III]λ9069	118.10	118.10	161.98

[1] average. [2] in km s^{-1}.

Table 4. FWHM measured in region R2b ΔX/ΔY: 17"-19"/17"-19".

	FWHM[1,2]	max FWHM[1,2]	max FWHM[2]
[O III]λ5007	231.31	276.70	414.29
HeIIλ5412	-	-	-
[Ar X]λ5533	419.93	419.93	419.93
[Fe VII]λ6087	-	-	-
[O I]λ6300	130.53	130.53	169.56
[S III]λ6312	-	-	-
[O I]λ6364	-	-	-
[Fe X]λ6375	317.62	317.62	431.50
Hα λ6563	212.09	302.18	502.65
[N II]λ6583	145.83	145.83	172.41
HeIλ6678	-	-	-
[S II]λ6716	139.08	145.08	222.67
[Ar V]λ7006	-	-	-
[Ar III]λ7136	117.63	117.63	147.07
[O II]λ7320	103.63	103.63	103.63
[S III]λ9069	-	-	-

[1] average. [2] in km s^{-1}.

Table 5. FWHM measured in region R3 ΔX/ΔY: 20"-25"/16"-19".

	FWHM[1,2]	max FWHM[1,2]	max FWHM[2]
[O III].λ5007	242.93	311.40	654.85
HeII.λ5412	-	-	-
[Ar x].λ5533	165.09	165.09	239.91
[Fe VII].λ6087	217.67	217.67	541.28
[O I].λ6300	137.28	137.28	254.49
[S III].λ6312	-	-	-
[O I].λ6364	-	-	-
[Fe x].λ6375	167.85	167.85	247.35
Hα .λ6563	223.04	315.90	502.65
[N II].λ6583	159.52	161.39	287.12
HeI.λ6678	-	-	-
[S II].λ6716	153.09	164.37	431.63
[Ar v].λ7006	137.14	137.14	203.06
[Ar III].λ7136	150.73	155.35	305.29
[O II].λ7320	109.65	109.65	164.40
[S III].λ9069	175.48	175.48	256.08

[1] average. [2] in km s^{-1}.

Table 6. FWHM measured in region R4 ΔX/ΔY: 4"-7"/8"-11".

	FWHM[1,2]	max FWHM[1,2]	max FWHM[2]
[O III].λ5007	194.89	217.95	317.95
HeII.λ5412	213.49	213.49	325.61
[Ar x].λ5533	236.47	236.47	344.75
[Fe VII].λ6087	224.46	237.48	541.28
[O I].λ6300	170.21	214.54	355.62
[S III].λ6312	198.70	198.70	426.15
[O I].λ6364	-	-	-
[Fe x].λ6375	204.29	204.29	437.36
Hα .λ6563	169.76	221.52	306.84
[N II].λ6583	167.60	217.07	307.90
HeI.λ6678	160.63	186.11	470.34
[S II].λ6716	143.90	173.15	241.78
[Ar v].λ7006	185.58	188.31	314.73
[Ar III].λ7136	146.03	184.46	282.23
[O II].λ7320	270.55	336.79	647.57
[S III].λ9069	125.74	140.00	184.42

[1] average. [2] in km s^{-1}.

Table 7. FWHM measured in region R5a ΔX/ΔY: 11"-14"/5"-7".

	FWHM[1,2]	max FWHM[1,2]	max FWHM[2]
[O III].λ5007	246.70	322.52	458.39
HeII.λ5412	194.59	194.59	285.53
[Ar x].λ5533	157.38	157.38	174.62
[Fe VII].λ6087	196.67	201.44	295.66
[O I].λ6300	197.52	262.98	486.07
[S III].λ6312	139.75	144.02	209.41
[O I].λ6364	-	-	-
[Fe x].λ6375	210.16	210.16	381.42
Hα .λ6563	226.96	317.83	489.60
[N II].λ6583	213.06	293.41	482.82
HeI.λ6678	187.75	187.75	352.43
[S II].λ6716	195.42	256.15	368.11
[Ar v].λ7006	201.52	201.52	401.66
[Ar III].λ7136	151.77	168.39	458.91
[O II].λ7320	222.81	247.85	647.57
[S III].λ9069	134.21	140.29	207.92

[1] average. [2] in km s^{-1}.

Table 8. FWHM measured in region R5b ΔX/ΔY: 15"-19"/5"-8".

	FWHM[1,2]	max FWHM[1,2]	max FWHM[2]
[O III].λ5007	241.61	310.98	654.85
HeII.λ5412	185.20	185.20	488.50
[Ar x].λ5533	292.35	292.35	447.36
[Fe VII].λ6087	177.53	179.65	325.64
[O I].λ6300	204.50	268.16	522.33
[S III].λ6312	165.16	173.30	522.33
[O I].λ6364	-	-	-
[Fe x].λ6375	256.48	256.48	530.82
Hα .λ6563	238.23	332.96	502.65
[N II].λ6583	224.92	311.84	502.65
HeI.λ6678	207.98	207.98	426.86
[S II].λ6716	193.17	255.07	491.36
[Ar v].λ7006	155.43	159.66	387.87
[Ar III].λ7136	172.32	203.44	462.73
[O II].λ7320	164.27	179.51	647.57
[S III].λ9069	161.72	185.80	363.64

[1] average. [2] in km s^{-1}.

Table 9. FWHM measured in region R6a ΔX/ΔY: 0"-1"/0"-1".

	FWHM[1,2]	max FWHM[1,2]	max FWHM[2]
[O III].λ5007	266.54	362.76	393.56
HeII.λ5412	165.43	165.43	203.56
[Ar x].λ5533	187.49	187.49	194.74
[Fe VII].λ6087	261.17	391.28	416.86
[O I].λ6300	195.78	267.54	300.10
[S III].λ6312	124.02	124.02	124.02
[O I].λ6364	162.66	201.91	222.50
[Fe x].λ6375	196.16	196.16	201.39
Hα .λ6563	236.59	350.79	367.16
[N II].λ6583	210.90	301.26	312.09
HeI.λ6678	282.17	448.87	494.12
[S II].λ6716	207.79	295.13	307.59
[Ar v].λ7006	172.40	202.81	232.23
[Ar III].λ7136	219.19	326.07	361.89
[O II].λ7320	146.09	153.17	184.16
[S III].λ9069	164.44	238.50	243.81

[1] average. [2] in km s^{-1}.

Table 10. FWHM measured in region R6b ΔX/ΔY: 3"-4"/4"-5".

	FWHM[1,2]	max FWHM[1,2]	max FWHM[2]
[O III].λ5007	264.12	357.91	383.07
HeII.λ5412	-	-	-
[Ar x].λ5533	579.34	579.34	579.34
[Fe VII].λ6087	200.24	200.24	206.85
[O I].λ6300	147.08	170.14	247.64
[S III].λ6312	-	-	-
[O I].λ6364	122.44	122.44	122.44
[Fe x].λ6375	243.09	243.09	459.43
Hα .λ6563	193.78	269.57	307.16
[N II].λ6583	187.13	250.60	348.42
HeI.λ6678	-	-	-
[S II].λ6716	195.90	273.22	335.07
[Ar v].λ7006	-	-	-
[Ar III].λ7136	196.58	285.60	462.73
[O II].λ7320	245.82	348.97	459.17
[S III].λ9069	208.45	208.45	226.24

[1] average. [2] in km s^{-1}.

Table 11. FWHM measured in region R7 ΔX/ΔY: 0"-5"/15"-20".

	FWHM[1,2]	max FWHM[1,2]	max FWHM[2]
[O III]λ5007	249.75	327.65	654.85
HeIIλ5412	-	-	-
[Ar X]λ5533	267.58	267.58	505.81
[Fe VII]λ6087	-	-	-
[O I]λ6300	131.75	132.91	219.62
[S III]λ6312	-	-	-
[O I]λ6364	-	-	-
[Fe X]λ6375	269.31	269.31	530.82
Hα λ6563	204.41	280.92	502.65
[N II]λ6583	155.42	180.21	375.20
HeIλ6678	136.23	136.23	177.78
[S II]λ6716	152.87	184.34	491.36
[Ar V]λ7006	-	-	-
[Ar III]λ7136	133.55	136.27	462.73
[O II]λ7320	114.38	114.38	175.10
[S III]λ9069	104.90	104.90	176.47

[1] average. [2] in km s^{-1}.

Table 12. FWHM measured in region R8 ΔX/ΔY: 15"-25"/0"-4".

	FWHM[1,2]	max FWHM[1,2]	max FWHM[2]
[O III]λ5007	254.62	323.29	654.85
HeILλ5412	-	-	-
[Ar X]λ5533	185.23	185.23	371.87
[Fe VII]λ6087	143.02	143.02	143.02
[O I]λ6300	168.02	177.55	380.05
[S III]λ6312	-	-	-
[O I]λ6364	-	-	-
[Fe X]λ6375	218.10	218.10	530.82
Hα λ6563	223.30	294.64	502.65
[N II]λ6583	173.35	189.60	294.05
HeLλ6678	-	-	-
[S II]λ6716	178.47	211.43	491.36
[Ar V]λ7006	211.18	211.18	295.03
[Ar III]λ7136	161.44	163.10	323.07
[O II]λ7320	104.71	104.71	122.15
[S III]λ9069	91.48	91.48	126.39

[1] average. [2] in km s^{-1}.